

1

2

The Low Resolution CCSM4

3

4

Christine A. Shields^{*}, David A. Bailey, Gokhan Danabasoglu,

5

Markus Jochum, Jeffrey T. Kiehl, Samuel Levis, Sungsu Park

6

National Center for Atmospheric Research, Boulder, CO

7

8

Revised Submission to Journal of Climate, CCSM4 Special Collection

9

December xx, 2011

10

11

12

13

** Corresponding author address:* 1850 Table Mesa Drive, Boulder, CO 80305

14

USA.

15

Email: shields@ucar.edu

Abstract

The low resolution version of the Community Climate System Model version 4 (CCSM4) is a computationally efficient alternative to the intermediate and standard resolution versions of this fully coupled climate system model. It employs an atmospheric horizontal grid of $3.75^{\circ} \times 3.75^{\circ}$ with 26 levels in the vertical with a spectral dynamical core (T31), and an oceanic horizontal grid that consists of a nominal 3° resolution with the 60 levels in the vertical. This low resolution version (T31x3) can be used for a variety of applications including long equilibrium simulations, development work, and sensitivity studies. The T31x3 model is validated for modern conditions by comparing to available observations. Significant problems exist for Northern Hemisphere Arctic locales where sea ice extent and thickness are excessive. This is, in part, due to low heat transport in T31x3 which translates into a globally averaged sea surface temperature (SST) bias of -1.54°C compared to observational estimates from the 1870-1899 historical record, and a bias of -1.26°C compared to observations from the 1986-2005 historical record. Maximum zonal wind stress magnitude in the Southern Hemisphere closely matches observational estimates over the ocean, although its placement, a reflection of the Southern Westerlies, is incorrectly displaced equatorward. Aspects of climate variability in the T31x3 compare to observed variability, especially so for ENSO where the amplitude and period approximate observations. T31x3 surface temperature anomaly trends for the 20th century also closely follow observations. An examination of the T31x3 model relative to the intermediate CCSM4 resolution (finite volume dynamical core 1.9°

37 x 2.5°) for pre-industrial conditions shows the T31x3 model to approximate this solution
38 for climate state and variability metrics examined here.

39

40

41

42

43

44

45

46

47

48

49

50

51

52

53

54 **1. Introduction**

55 As global climate models become increasingly sophisticated, so does the need for
56 computing power and resources. Historically, the Community Climate System Model
57 (CCSM) modeling community has supported several resolutions, including a
58 computationally efficient lower resolution version designed for applications requiring
59 long integrations. (Boville and Gent, 1998; Otto-Bliesner et al 2002; Yeager et al 2006).
60 The latest CCSM release, (CCSM4), is no different. This paper presents a low resolution
61 CCSM4 as an alternative to the higher resolution versions and highlights both its
62 strengths and weaknesses in comparison with observations and other CCSM4 resolution
63 versions.

64

65 CCSM4 contains several notable improvements spanning all model components which
66 include a much improved El Nino/Southern Oscillation (ENSO) representation, improved
67 ocean mixing, a new land carbon-nitrogen (CN) component, more realistic ice albedos,
68 and new coupling infrastructure. The low resolution CCSM4 (henceforth called T31x3)
69 uses a T31 spectral dynamical core for the atmospheric and land components
70 (horizontal grid of $3.75^\circ \times 3.75^\circ$) with 26 atmospheric layers in the vertical. The ocean
71 and ice components employ a nominal 3° irregular horizontal grid (referred to as x3)
72 with 60 ocean layers in the vertical. The intermediate resolution CCSM4 utilizes the
73 finite-volume (FV) dynamical core (Lin 2004) with a nominal 2° atmosphere and land
74 horizontal grid ($1.9^\circ \times 2.5^\circ$ latitude versus longitude) with 26 atmospheric layers in the

vertical, and a nominal 1° ocean and ice horizontal grid (referred to as x1) with 60 ocean layers in the vertical, (henceforth called FV2x1). The standard CCSM4 resolution applies the finite volume dynamical core with a 1° atmosphere ($0.9^\circ \times 1.25^\circ$ latitude versus longitude) with the same number of vertical levels coupled to the x1 ocean and ice models, (henceforth called FV1x1). Further details on CCSM4 model improvements and specifics about the higher resolution simulations can be found in Gent et al. (2011).

As indicated above, the low resolution version of CCSM4 uses a spectral dynamical core rather than the finite volume dynamical core used by other CCSM4 resolutions.

Jablonowski and Williamson (2006) found that a low resolution finite volume version ($4^\circ \times 5^\circ$, latitude versus longitude) was too coarse to resolve baroclinic eddies and thus a major barrier to tropospheric climate studies. The minimum resolution necessary to sufficiently simulate storm systems with the finite volume dynamical core is found to be $2.5^\circ \times 3.3^\circ$ at nearly double the cost compared to T31 (Lauritzen, pers. communication).

Although the finite volume dynamical core may be optimal for tracer transport applications, including chemistry, given the need to provide the community with a computationally affordable alternative, the T31 spectral dynamical core was chosen for the atmosphere.

There are a number of physics differences in the T31x3 version of the model compared to the other CCSM4 resolutions. Minor cloud parametric changes (necessary to achieve

radiative balance) are applied to the atmospheric component as well as and the inclusion of a turbulent mountain stress (TMS) parameterization. Ice albedo and some ocean parameter settings are changed in the ice and ocean components, respectively. In the land component, the ice runoff parameterization is not used. Here we present an overview of the simulations for each model component as well as review of the impact of resolution. Although all three CCSM4 resolutions are discussed in section 4, the majority of the paper places emphasis on the comparison between the low and the intermediate resolutions of the model and comparisons to observation (section 5). Model variability, in particular, ENSO, Northern Annular Mode (NAM), and Southern Annular Mode (SAM) are presented in section 6 along with a brief word on climate sensitivity in section 7. Finally, computational model performance statistics are presented to highlight the major cost savings associated with T31x3. This paper is not intended to be a comprehensive paper documenting all aspects of the T31x3 (or the FV2x1) simulation. Rather, it simply shows that the T31x3 is an alternative to the more costly FV2x1 by presenting a sample of basic climate state and variability metrics in comparison with available observations.

2. Model Description and Physics Differences from standard CCSM4

CCSM4 is a fully coupled, global climate model consisting of atmosphere, land, ocean, and sea ice components as well as a coupler that passes state and flux information between the model components. A detailed description of the modeling system and

117 each model component can be found in the J. Climate CCSM4 Special Issue Collection
118 and include papers by Gent et al. (2011) (overview), Neale et al. (2011), (atmosphere),
119 Lawrence et al. (2011) (land), Danabasoglu et al. (2011) (ocean), and Holland et al.
120 (2011) and Jahn et al. (2011) (ice).

121

122 The atmosphere component is the Community Atmosphere Model Version 4 (CAM4)
123 (Neale et al. 2011). Aside from the dynamical core differences discussed in the
124 introduction, another important difference between the T31x3 and all other CCSM4
125 resolutions is the inclusion of the TMS (turbulent mountain stress) parameterization in
126 CAM4 which significantly improves the coupled atmosphere-ocean interactions. TMS
127 improves ocean surface stress in the low resolution model and will be discussed further
128 in sections 4 and 5. Although TMS was available in earlier versions of CAM, up until now,
129 it has only been invoked within the Whole Atmosphere Community Climate Model
130 (WACCM). TMS in WACCM was applied to better handle gravity waves in the upper
131 atmosphere by improving the representation of sub grid-scale mountain ranges.
132 Following the treatment of regular surface stress, CCSM4 assumes that the topography-
133 induced roughness length is proportional to the standard deviation of sub-grid
134 topographic heights within the grid. The resulting neutral drag coefficient decreases
135 linearly with stability. In the stable regime, drag coefficient is down to zero where
136 gradient Richardson number in the two lowest model layers is 1. Details about the
137 origin of TMS parameterizations can be found in Klinker and Sardeshmukh (1992) and

Milton and Wilson (1996). Another difference between the T31 version of CAM4 and the standard CAM4 is the adjustment of cloud processes parameters. The relative humidity and autoconversion thresholds were slightly modified to achieve radiative top-of-atmosphere (TOA) balance for pre-industrial conditions. Altering properties in the cloud parameterization scheme has been well documented in previous versions of CCSM (Yeager et al. 2006; Williamson 1995; Hack et al. 2006) and continues to remain valid for CAM4. All resolution versions of CCSM4 include cloud parameter adjustments to achieve TOA balance and minimize drift in the coupled model.

The land component of CCSM4 is the Community Land Model version 4 (CLM4; Lawrence et al. 2011). Although there are no resolution-dependent physics differences, the T31x3 version of CCSM4 does not account for the latent heat flux associated with snow and ice melt into liquid runoff. This is in contrast with the other resolution CCSM4 versions where the liquid and ice runoff amounts are kept track separately and the ocean model loses heat during the phase conversion from ice to liquid runoff. For the x3 ocean resolution, this approach created a problem in some isolated regions, e.g., the Baffin Bay region, where the ocean model continuously gets ice runoff and therefore continuously loses heat at the surface. Without adequate advective transport due to the coarse model grid, these cold regions stay local, leading to continuous ice formation with rather thick ice. Therefore, we chose to attain a more reasonable ice thickness at the expense of energy conservation in the released T31x3 model. The total runoff is

159 always accounted for regardless of how ice runoff is treated. We also note that no CCSM
160 version takes into account the temperature of the runoff water.

161

162 The CCSM4 ocean component is the Parallel Ocean Program version 2 (POP2; Smith et
163 al. 2010, Danabasoglu et al. 2011). The coarse resolution configuration presented here
164 uses the same nominal 3° horizontal grid described in Yeager et al. (2006) for CCSM3.
165 However, the number of vertical levels has been increased from 25 levels in CCSM3 to
166 60 levels in the present x3 configuration. The associated vertical grid spacing is the same
167 as the one employed in the x1 ocean model used in the standard CCSM4 version, thus
168 allowing us to use the same prescriptions for the vertical mixing coefficients in all
169 resolution versions. Due to this change in the vertical resolution, the discrete bottom
170 topography was recreated using a smooth (one pass of a 9-point Gaussian filter) version
171 of the 2-minute gridded global relief data (ETOPO2v2 2006). As in the x1 version, the
172 minimum and maximum ocean depths were set to 30 and 5500 m, respectively, and
173 isolated holes were eliminated. Additional changes were then incorporated. These
174 include the Denmark Strait, Faroe Bank Channel, Weddell Sea, and Ross Sea overflow
175 regions to accommodate the numerical requirements of an overflow parameterization
176 as discussed in Danabasoglu et al. (2011). Furthermore, the Samoa Passage was
177 widened to improve deep ventilation in the Pacific basin. Also, as in the x1 CCSM4
178 configuration, but in contrast with the x3 CCSM3, the Gibraltar Strait was opened with a

cliff-topography to its immediate west to explicitly allow the Mediterranean overflow into the Atlantic basin.

All the new physics developments and changes described in Danabasoglu et al. (2011) are used in the x3 configuration with the following differences from the x1 configuration: the upper-ocean lateral tracer diffusivity coefficients are increased to $4000 \text{ m}^2 \text{ s}^{-1}$ (from $3000 \text{ m}^2 \text{ s}^{-1}$) and the anisotropic horizontal viscosity coefficients are oriented along the model grid directions (instead of the east-west and north-south directions) with larger values. These larger viscosities are simply due to the coarser horizontal resolution of the x3 configuration. We note that there are three aspects of the horizontal viscosity formulation that are still the same between x3 CCSM3 and CCSM4 configurations: overall viscosity values, their grid-dependent orientations, and no dependency of these viscosities on the local deformation rate. The present x3 uses the same third-order upwind tracer advection scheme as in the x1 CCSM4 instead of the centered advection scheme of the x3 CCSM3. Finally, CCSM4 x3 now includes the parameterized diurnal cycle in shortwave heat flux unlike in the x3 CCSM3.

The CCSM4 sea ice component is based on the Community Ice Code version 4 (CICE4) (Hunke and Lipscomb 2008, Holland et. al, 2011). Adjustments to ice albedos were required to simulate more reasonable ice extent and thickness values. Ice albedos designed for the x1 model are not appropriate for the low resolution model and were

decreased to compensate for excessive ice. In CCSM4, ice albedos are not adjusted directly, but are computed using parameters representing optical properties of snow, bare sea ice, and melt ponds. These values are based on standard deviations from data obtained by SHEBA (Surface Heat Budget of the Arctic), (Uttal et. al 2002).

3. Overview of simulations

Two T31x3 simulations are presented; a pre-industrial control simulation (1850 AD forcing) of 500 years in length, and a modern 20th century transient simulation (1850 - 2005 AD forcing). In sections 4 and 6, the T31x3 pre-industrial simulation is compared to the FV2x1 pre-industrial control as a means to show the viability of the T31x3 model as an alternative to the FV2x1 model. However, in order to evaluate the T31x3 model with respect to nature, in section 5, we analyze the modern period (1986-2005) of the 20th century simulation compared to observations. We will refer to the low resolution pre-industrial simulation as T31x3_1850, the low resolution 20th century simulation as T31x3_20C, the intermediate and standard Pre-Industrial simulations as FV2x1_1850 and FV1x1_1850, and the intermediate and standard 20th century simulations as FV1x1_20C and FV2x1_20C. Further details on FV1x1 and FV2x1 control and 20th century simulations can be found in Gent et al. (2011).

The T31x3_1850 control simulation was initialized using PHC2 potential temperature and salinity data (Polar Science Center Hydrographic Climatology dataset, representing a blending of the Levitus et al (1998) and Steele et al. (2001) data for the Arctic Ocean) and state of rest in the ocean model. The 20th century simulation was integrated for 150 years using aerosol, greenhouse gas, volcanic, solar, land use, and nitrogen deposition forcing suitable for the historical period of 1850 – 2005 AD. This run was initialized from the T31x3_1850 control simulation at year 500. Unless otherwise stated, figures for mean state variables in this paper will use a 50 year average taken from the end of each pre-industrial control simulation, and the last 20 years (1986-2005) for the 20th century simulations.

The decision was made to tune the T31x3 model to achieve a near zero TOA balance for 1850 conditions, in step with all other CCSM4 pre-industrial control simulations (FV1x1_1850 and FV2x1_1850) documented in Gent et al. (2011). After tuning, the T31x3_1850 control simulation was integrated for 500 years but essentially came into a stable TOA radiative balance after 100 years of integration. The mean TOA heat imbalance computed using the last 50 years is $+0.09 \text{ W m}^{-2}$. Following an initial, rapid decline, the ocean global volume-mean potential temperature, $\langle T \rangle$, increases almost linearly starting at year 50 (Fig. 1a). By the end of the 500-year T31x3_1850 simulation, $\langle T \rangle$ is 3.80°C , representing a warming of about 0.10°C from its initial value. The oceanic heat gain remains rather steady at 0.16 W m^{-2} ($= 0.11 \text{ W m}^{-2}$ when scaled by the entire

240 surface area of the Earth) after the initial transient and largely reflects the TOA heat gain
 241 of 0.09 Wm^{-2} in the coupled system. In comparison with the initial condition, most of
 242 this heat gain occurs in the 500-3500 m depth range while the ocean loses heat above
 243 500-m depth (not shown). We note that the heat gain in T31x3_1850 is in stark contrast
 244 with both FV1x1_1850 and FV2x1_1850 in which the ocean actually loses heat at -0.14
 245 W m^{-2} (over the last 700 years) and -0.09 W m^{-2} (over the last 600 years), respectively.
 246 The ocean global volume-mean salinity, $\langle S \rangle$, shows a small, but linear freshening trend
 247 after year 50, corresponding to $-2.9 \times 10^{-4} \text{ psu century}^{-1}$ for years 50-500 (Fig. 1b).
 248 Nevertheless, due to the initial salt gain, $\langle S \rangle$ at year 500 is only $4 \times 10^{-4} \text{ psu}$ fresher than
 249 its initial value. Similar freshening with comparable trends is also seen in FV1x1_1850,
 250 while FV2x1_1850 does not show any monotonic and discernable trends in $\langle S \rangle$.

251

252 An important metric for a coarse resolution coupled model is to have a stable
 253 meridional overturning circulation, particularly in the Atlantic Basin (Yeager et al. 2006).
 254 We show the Atlantic Meridional Overturning Circulation (AMOC) maximum transport
 255 time series from T31x3_1850 in Fig. 1c. Here, the maximum transport is searched for
 256 below 500-m depth and between 30° - 60°N and it includes parameterized eddy
 257 contributions in addition to the mean flow. Following an initial decline, the model
 258 maintains a robust AMOC with a mean maximum transport of 17.4 Sv over the last 100
 259 years. This transport, however, is smaller than in both FV1x1_1850 ($\sim 26 \text{ Sv}$) and
 260 FV2x1_1850 (~ 26 and $\sim 23 \text{ Sv}$ in high and low transport regimes, respectively).

261

262 **4. Resolution Differences**263 *a. Ocean SST and Zonal Wind Stress*

264 The T31x3_1850 sea surface temperature (SST) difference distribution from the Hurrell
 265 et al. (2008) dataset is presented in Fig. 2 in comparison with the FV1x1_1850 and
 266 FV2x1_1850 differences from the same observational data. For these pre-industrial
 267 comparisons, the observational estimate is based on the 1870-1899 time-mean SST. In
 268 T31x3_1850, the global-mean SST bias is -1.54°C , colder than in both higher resolution
 269 versions. The root-mean-square (rms) difference of 2.28°C from observations in
 270 T31x3_1850 also represents the largest departure from observations among these
 271 control cases. The warm bias magnitudes in the upwelling regions off the west coasts of
 272 South America, South Africa, and California are comparable in T31x3_1850 and
 273 FV1x1_1850 – in both these biases are smaller than in FV2x1_1850. The largest cold
 274 biases in excess of 6°C occur in the North Pacific and North Atlantic in T31x3_1850.
 275 These are due to more southerly paths of the Kuroshio and Gulf Stream / North Atlantic
 276 Currents and subsequent too-far-south penetration of the subpolar gyres in both basins,
 277 and they are noticeably different than those of FV1x1_1850 and FV2x1_1850. These
 278 differences primarily reflect changes in the barotropic circulation partly resulting from
 279 differences in the wind stress curl fields that largely determine the interior gyre
 280 circulation through the Sverdrup balance in these coarse resolution simulations
 281 (Danabasoglu 1998). In particular, the T31x3_1850 wind stress curl exhibits a subpolar

positive pattern with significantly more southward excursion than in FV1x1_1850 and FV2x1_1850 (not shown).

Zonal averages of the zonal wind stress component from pre-industrial and 20th Century simulations for the Southern Hemisphere are presented in Fig. 3 (discussion of the 20th Century results is deferred to Section 5b). Both pre-industrial simulations with the FV dynamical core show very similar distributions with similar maximum wind stresses ($> 0.19 \text{ N m}^{-2}$) located at about 54°S , indicating little sensitivity to the horizontal resolution of the atmospheric model. In comparison, the Southern Hemisphere storm track is displaced further north and its maximum strength is smaller (0.14 N m^{-2} located at 47°S) in T31x3_1850. The TMS parameterization appears to contribute to this weakened wind stress as a sensitivity simulation (referred to as T31x3_1850_NOTMS in Fig. 3) shows roughly 10% larger magnitudes without it.

b. Precipitation and River Transport

Annual averaged precipitation rate across different model horizontal resolutions (Fig. 4) is shown for the 1850 control runs. All three resolutions exhibit the signature double-ITCZ (inter-tropical convergence zone) also seen in CCSM3 (Hack et. al 2006) and previous versions of the model, regardless of dynamical core. In general, precipitation rate and precipitable water (not shown) is reduced in T31x3 compared to both FV2x1

and FV1x1 as evidenced by a globally averaged value of 2.64 mm/day of precipitation rate for T31x3 as opposed to values of 2.93 and 2.87 for FV2x1_1850, and FV1x1_1850, respectively. Spatially, this can be seen in Fig. 4 with the largest differences in the tropical Pacific. In part, this can be attributed to the fact that the T31x3 is a colder model (Figs. 2 and 8) than its higher resolution counterparts, so less precipitable water is available to the system. Less precipitation improves the comparison to observations in the 20th Century run (discussed in section 5a) which in turn improves sea surface salinity biases (section 5c).

River flow acts as an integrator of processes across river basins. Such processes include mass and energy exchange at the land-atmosphere interface, in the soils, and in plants. Gent et al. (2010) evaluated 2° and 0.5° pre-industrial simulations of the CCSM3.5 by analyzing the river flow simulated by the CLM's river transport model. Gent et al. (2010) found improved river flow at higher resolution and attributed this mainly to the improved simulation of atmospheric variables in CAM, and to a lesser degree to the improved representation of land surface processes, such as snow cover, in the CLM. Following a similar approach here, we assess whether the T31x3_1850 simulation shows degraded river transport relative to the FV2x1_1850 simulation. For the most part, it does not. Cumulatively, the T31x3 model underestimates and the FV2x1 and FV1x1 models overestimate fresh water input to the Northern Hemisphere oceans relative to observational estimates (Dai and Trenberth 2002) (Fig. 5a). The FV2x1_1850 model is in

closer agreement to the global total observed runoff, partly due to compensating biases. The T31x3_1850 model performs better than the FV2x1_1850 in the Atlantic Ocean basin (Fig. 5b) and better than both FV models in the Indian Ocean basin (Figure 5c), although the T31x3_1850 model underestimates runoff in the northern Indian Ocean. In the Pacific Ocean basin it is more difficult to pick the better simulation (Fig. 5d). These changes can be attributed to increased precipitation in the T31x3_1850 simulation in the Amazon Basin and near the 30N^o-40N^o latitude band, and decreased precipitation in monsoon regions surrounding the Indian Ocean (Fig. 4). The T31x3_1850 model shows a sharp reduction in Arctic runoff relative to the FV models (Fig. 5e) due to a strong high-latitude cold bias at T31x3 (Fig. 2 and 8). Colder temperatures are accompanied with reduced precipitation (Fig. 4). Colder temperatures also lead to the accumulation of water in perennial soil ice (not shown).

c. Sea Ice and Northward Heat Transport Impact

A key result when analyzing sea ice across resolutions (Fig. 6) is that the ice extent in the Arctic improves with resolution. This is mostly due to an improvement in the Northern Hemisphere winds (not shown) and atmospheric and oceanic heat transport with resolution. Note the sea ice is too extensive in both the T31x3 and FV2x1 simulations (Fig.6 upper panels) compared to the SSM/I satellite observations (Cavalieri, 1996) (solid black line) and by contrast well simulated in the FV1x1 simulation. When evaluating sea ice extent timeseries across the entire length of the 1850 control simulations, we find

the FV2x1 simulation produces a sea ice pattern in the Labrador Sea very similar to FV1x1 (not shown) during some time periods, while most time periods exhibit a spatial extent as seen in Fig. 6. In both the T31x3 and FV1x1, the sea ice extent is stable and similar across all years in the control experiments. The Southern Hemisphere sea ice area is shown in Fig. 6, lower panels. The summer (JFM) minimum extent and area in the T31x3_1850 simulation are closer to SSM/I satellite observations (Fig. 6, lower panels) than either the higher resolution versions. Similarly, the sea ice is thinner overall in T31x3_1850 and more in agreement with the sparse observational estimates of Southern Hemisphere sea ice thickness (not shown).

The relatively poor performance of the model in representing the Northern Hemisphere sea ice compared to the Southern Hemisphere sea ice is due to different processes. In the northern hemisphere it is accomplished by coastal boundary currents, which are neither resolved nor parameterized. This leads to a too small poleward heat transport in the Arctic. With higher resolution, resolving these coastal currents leads to a redistribution of heat and a reduced sea ice bias in the Northern Hemisphere (Jochum et al. 2008). In the Southern Hemisphere, the sea ice distribution becomes worse with higher resolution due to the fact that the Southern Hemisphere westerlies are overly strong (Holland and Raphael, 2006). Why these westerlies become stronger and worse as the resolution increases is an open question since Boville (1991). Bitz et al. (2005) also discusses important factors in determining ice extent in observations and models.

365

366 These concepts are nicely demonstrated in the various CCSM4 simulations. Poleward
367 heat transport in the x3 ocean is lower than both observationally-based estimates and
368 the higher resolution simulations in the Northern Hemisphere while similar to the x1
369 ocean in the Southern Hemisphere (see Fig. 15). This is also true of the northward heat
370 transport by the atmosphere (not shown). The magnitude of the Southern Hemisphere
371 wind stress in the x3 ocean compares better to observational estimates than the higher
372 resolution models which are all too high (Fig. 3). The equatorward displacement of the
373 wind stress in the x3 ocean is corrected somewhat by the inclusion of the TMS
374 parameterization (Fig. 3). It is important to note that neither the intermediate or
375 standard resolution experiments apply TMS. Given the Southern Hemisphere poleward
376 heat transport is similar at all resolutions, the likely explanation for the improvement in
377 Antarctic sea ice extent is due to the improvement in the wind stress. In the northern
378 hemisphere, the weak northward heat transport in the atmosphere and ocean explains
379 the thicker and more extensive sea ice in the low resolution CCSM4. Other work (Bitz
380 pers. comm.) on the ultra-high resolution CCSM4 show a high bias in northward heat
381 transport (atmosphere and ocean). Consequently, in the Northern Hemisphere, sea ice
382 is too thin and extent too low, while the Southern Ocean extent is similar to other
383 resolutions due to a similar bias in the surface wind stress.

384

385

d. 20th Century Surface Temperature Anomalies

When comparing the 20th century simulations across resolutions, surface temperature anomalies are examined. Anomalies are computed using the mean of the first 20 years of each case (Fig. 7) following Gent et al., (2011). The T31x3 timeseries tracks closely with the observational record (HadCRUT3v) and the FV1x1_20C. The FV2x1_20C is an outlier in that the surface temperature anomalies are greater than observed. By the end of the 20th century period, the T31x3 anomalies compare more closely to the observations than either the FV2x1_20C or the FV1x1_20C anomalies, yet are still slightly biased high. This result is consistent with Gent et al. (2011) which shows the CCSM4 response to the late 20th century historical forcing to be too strong.

5. Climate State and Comparison to Observations

a. The Atmosphere and Land Solutions

There are a number of systematic biases in the atmospheric simulation that are documented here. The bias in simulated annual, zonal-mean land surface air temperature is shown in Fig. 8. For the 20th Century simulation, the simulated surface air temperature is too cold (by 2° to 5°C) compared to the observations. The cold surface air temperature bias in the tropical regions is related to a deficit of incoming shortwave radiation in this region (not shown), where the energy deficit is as large as 30 to 40 Wm⁻² in certain regions. At higher Northern latitudes, the cold bias in the model is

related to weak ocean heat transport (see Fig. 15) compared to observations. Fig. 8 also indicates that the T31X3_1850 simulation is significantly colder over most latitudes than the FV2X1_1850 simulation, which is again indicative of biases in both the simulated surface energy budget and weak poleward heat transport in the T31X3 model.

To further investigate the role of biases in surface energy and ocean heat transport, a sensitivity study was carried out to test whether addressing the tropical surface energy bias could lead to an improvement in overall meridional surface air temperatures. The regional bias in absorbed shortwave energy in the tropical Atlantic ranges from 30 to over 40 Wm^{-2} , where the model underestimates shortwave energy absorbed at the ocean surface. One hypothesis is that this under representation of shortwave energy at the surface is linked to high latitude cold surface temperatures, because this missing tropical energy is not available to be transported to higher latitudes. To test this hypothesis, cloud properties were tuned to allow more shortwave radiation to reach the tropical surface, thus forcing the model to agree better with observational estimates of the surface shortwave budget (to locally within 10 Wm^{-2} of observations). The tropical surface-air temperatures from this re-tuned model did increase (in fact they were too warm compared to observational estimates by over 2°C), but high latitude temperatures remained too cold compared to observations, similar to the control version of the model. This result indicates that even if one were to improve the local shortwave bias in the tropical surface energy budget, the x3 ocean model cannot

efficiently transport this heat poleward to reduce the cold bias at high latitudes (see Fig. 15).

The bias in 20th century simulated annual mean precipitation (Fig. 9) illustrates the signature of a double ITCZ structure in the tropical Pacific which exists in all resolution versions (Fig 4.) Although the T31x3 compares to other resolutions, regional biases specific to the low resolution version certainly exist. There is a significant bias in the location of the maxima in the Indian monsoon (seen in June-July-August), where more precipitation occurs in the Arabian Sea region compared to the Bay of Bengal. There is also excessive precipitation in the Western Pacific warm pool region leading to low salinities in this region (see Fig. 13). Precipitation in the Congo region is also a significantly overestimated, which correlates through enhanced runoff with a low salinity bias in the southern Atlantic coastal region off of Africa (see Fig. 13).

The T31X3_20C zonal annual mean atmospheric temperature structure has many realistic features compared to reanalysis (Kalnay et al. 1996) as shown in Fig. 10. The comparison (Fig. 10c) shows the well-known bias signature of a cold polar upper troposphere of magnitude 7 to 8°C, a feature that has existed in previous versions of the CCSM regardless of resolution, (Collins et al. 2006, Neale et al. 2011). The atmosphere, in general, is too cold compared to the reanalysis. Comparison with other reanalysis products and satellite data (not shown) confirm this general feature of the model. The

tropical tropopause region also is too cold by $\sim 7^{\circ}\text{C}$, which will affect the model's ability to simulate realistic stratospheric water vapor.

The T31X3_20C annually averaged zonal mean wind is shown in Fig. 11. Note that in the Southern Hemisphere the jet is displaced too far equatorward, which is reflected in the bias in the zonal surface stress (Fig. 3). The equatorward displacement of the jets is a signature of the low resolution model. With increased horizontal resolution the southern hemisphere jet strengthens and shifts poleward.

The simulated Northern Hemisphere 500 hPa height field is compared to reanalysis in Fig. 12. The T31X3_20C simulation of the Pacific Northwest ridge is in better agreement than the higher resolution simulations (not shown). This improvement may be due to the TMS parameterization, but also could be related to the position of tropical Pacific heating given that this ridge is related to Rossby wave propagation from the central Pacific region. The biases in the simulated height field of the North Atlantic region points to biases in the Arctic circulation that exacerbate biases in Arctic sea ice thickness and extent (see Figs. 6 and 16).

Finally, for land model diagnosis, we evaluate river discharge as in Section 4. Here we add the T31x3_20C simulation to the comparison shown in Fig. 5. We find that in all

ocean basins except the Pacific the T31x3_20C simulation performs similar to or better than the three 1850 configurations relative to the observations. This statement holds primarily for the cumulative ocean basin discharge values and is reassuring considering that the observations correspond to the present day.

b. The Ocean Solution

The SST and sea surface salinity (SSS) differences from the present-day Hurrell et al. (2008) dataset (1986-2005 mean) and the Polar Science Center Hydrographic Climatology (PHC2; a blending of the Levitus et al. (1998) and Steele et al. (2001) data for the Arctic Ocean), respectively, are shown from T31x3_20C in Fig. 13. The global-mean SST is colder than in observed by -1.26°C and the associated rms difference is 1.88°C . These can be contrasted with the corresponding FV1x1_20C values of 0.30°C and 1.14°C , respectively. The present-day SST difference patterns and most magnitudes are very similar to those of the pre-industrial control simulation (Fig. 2c). The largest exception is the reduced cold bias in the North Pacific. The SSS difference distribution shows a substantial reduction of the fresh bias in T31x3_20C compared to FV1x1_20C with mean biases of -0.15 and -0.37 psu, respectively. The rms error in T31x3_20C (0.94 psu) is very similar to that of FV1x1_20C (0.88 psu). We believe that the reduced fresh bias in T31x3_20C largely reflects the improvements in precipitation with much reduced mean and rms errors compared to observations than in the higher resolution versions.

489 The AMOC remains rather robust throughout T31x3_20C with its maximum transport
490 fluctuating roughly between 15.5 and 19.5 Sv (not shown). As in the FV1x1_20C
491 simulations, the maximum transport diminishes only slightly by 1-2 Sv towards the end
492 of the 20th Century. For this later period (1986-2005), Fig. 14 presents the time-mean
493 global and Atlantic MOC distributions for the total flow, showing generally weaker
494 transports in T31x3_20C than in both the higher resolution versions and available
495 observations. For example, the cell associated with the North Atlantic Deep Water
496 (NADW; large clockwise circulation in the Northern Hemisphere in both panels) has a
497 maximum transport of 16.8 Sv, smaller than the FV1x1_20C transport of 24 Sv. At the
498 latitude of the RAPID observations (26.5°N), the AMOC maximum transport is about
499 13.5 Sv, lower than the observational mean transport estimate of 18.7 Sv (Cunningham
500 et al. 2007). In T31x3_20C, the combined Denmark Strait and Faroe Bank Channel
501 overflow transport is also low, i.e., 3 Sv, compared to available observational estimates
502 (6.4 – 9.4 Sv) and that of the FV1x1_20C (5.2 Sv). Despite the parameterized overflows,
503 the penetration depth of the NADW remains shallow. Here, this depth is defined as the
504 depth of the zero contour line, separating the NADW cell from that of the Antarctic
505 Bottom Water (AABW; counter-clockwise circulation below about 3000 m depth in Fig.
506 14b). Indeed, while the RAPID observations show about 4350 m as the NADW
507 penetration depth at 26.5°N, T31x3_20C penetration depth is only 3250 m, more than
508 1000 m shallower. Such shallow NADW penetration depths appear to be a common
509 feature of other CCSM4 simulations due to coupled model density biases in the North
510 Atlantic, as discussed in detail in Danabasoglu et al. (2010) and Danabasoglu et al.

511 (2011). Finally, the transport associated with the AABW is weaker in T31x3_20C (> 4 Sv
 512 global) than in both FV1x1_20C (> 8 Sv global) and the range of observational estimates.
 513 We refer to Danabasoglu et al. (2011) for further discussion on MOC.

514

515 In FV1x1_20C, the model deep water formation sites in the North Atlantic include the
 516 Labrador Sea basin in good agreement with observational estimates of deep convection
 517 sites. Unfortunately, this improvement is absent in T31x3 simulations where the main
 518 deep convection site is located just south of Iceland (not shown). Furthermore, both the
 519 geographical extent of the region with for example, mixed layer depths (MLD) > 250 m,
 520 and the mean maximum MLD are much smaller in T31x3_20C than in FV1x1_20C. These
 521 MLD changes along with weaker NADW transport cannot be attributed to coupled
 522 model biases as they are also present in forced ocean-only simulations at this
 523 resolution. Although a deeper discussion of ocean ventilation is beyond the scope of
 524 this paper, an in-depth analysis of the x3 ocean ventilation in comparison with the x1
 525 model and observations is available elsewhere, (K. Moore, personal communication).

526

527 We show the global and Atlantic Ocean total northward heat transports (NHT) from
 528 T31x3_20C in comparison with those of FV1x1_20C and the implied transport estimates
 529 from Large and Yeager (2009) based on the observationally-based surface flux data for
 530 the 1984-2006 period in Fig. 15. An Atlantic Ocean estimate using the RAPID data from
 531 Johns et al. (2011) is also included. As in the CCSM3 low resolution version, NHT in the

532 Atlantic Ocean is lower than either the implied estimate or in FV1x1_20C. The peak
 533 transport reaches only 0.66 PW located between 17°-23°N. The ocean model is likely
 534 responsible for this deficiency that accompanies weaker AMOC because forced ocean-
 535 only simulations produce similar or slightly larger NHT in the Atlantic Basin. The global
 536 NHT however remains closer to the implied estimate range due to a larger contribution
 537 from the Pacific domain. While the FV1x1_20C and T31x3_20 NHTs are almost the same
 538 with similar departures from the implied estimate between 15°S-10°N, NHT in
 539 T31x3_20C compares more favorably with the implied estimate than in FV1x1_20C
 540 south of 15°S.

541

542 Zonal-mean zonal wind stress maximum of 0.15 N m^{-2} in T31x3_20C is in excellent
 543 agreement with the estimate from Large and Yeager (2009) (Fig. 3). However, the model
 544 shows an unrealistic migration of the Southern Hemisphere storm track toward the
 545 equator as in the low resolution pre-industrial simulation. Due to this northward shift,
 546 the Antarctic Circumpolar Current transport at Drake Passage is only 105 Sv, lower than
 547 the Cunningham et al. (2003) observational estimate of 137 ± 8 Sv. In FV1x1_20C, while
 548 the latitude of the maximum zonal-mean zonal wind stress is in agreement with the
 549 Large and Yeager (2009) data, its magnitude is > 30% larger.

550

551 The larger lateral viscosities required by the model's low horizontal resolution produce
 552 wider western boundary currents with generally smaller transports compared to those

of the higher resolution versions. In the Pacific Ocean, the Equatorial Undercurrent compares favorably with the Johnson et al. (2002) observations with both its maximum zonal speed (100 cm s^{-1}) and the depth and upward tilt from west-to-east of its core (not shown). Finally, compared to observations, while the mean SST is colder by $1\text{-}2^{\circ}\text{C}$ along the equatorial Pacific (Figure 2), the SST seasonal cycle is in good agreement.

c. The Sea Ice Solution

The quality of the modern sea ice simulation in the low resolution CCSM4 is somewhat mixed. Overall, while the sea ice thickness and extent in the Southern Hemisphere are in agreement when compared to sparse observations, the distribution of the sea ice in the Northern Hemisphere is not correct. Fig. 16 (upper panels) show a comparison of the winter (JFM) maximum ice area for the T31x3_20C and FV1x1_20C transient simulations for the period of 1986-2005 for the Northern Hemisphere. The black contours show the 10% concentration line from SSM/I satellite (Cavalieri et al. 1996) observations. The FV1x1_20C produces the best overall ice extent for the Arctic while the T31x3_20C simulation is much too extensive. Jahn et al. 2011 found that although FV1x1_20C produces the spatial distribution quite well compared to observations, ice thicknesses are still biased high. The JFM sea ice thicknesses in Fig. 16 (lower panels) highlight the degradation in T31x3_20C. Part of the excessive thickness problem in the Arctic can be attributed to the TMS parameterization based on a sensitivity study without TMS that produced $\sim 20\%$ less ice in the Arctic Ocean. Unfortunately, even

574 without TMS, ice thicknesses were still too large. When developing the T31x3 model, we
575 found that omitting ice runoff from land alleviates some of the thickness bias in T31x3,
576 particularly over the Baffin Bay region. Lowering inherent optical properties for the
577 snow on sea ice, i.e. reducing the surface albedo, also helps to improve the overall
578 thickness bias in the Arctic, but ultimately, even with these changes, all T31x3
579 simulations produce much too thick sea ice in the Arctic.

580

581 In the Southern Hemisphere (Figure 16, middle panels), as in the 1850 control
582 simulations, the summer (JFM) sea ice extent is greatly improved in the T31x3_20C
583 simulation compared to the Northern Hemisphere. While both simulations are too
584 extensive in summer compared to SSM/I satellite observations, the T31x3_20C produces
585 a more reasonable ice extent compared to the higher resolution version.

586

587 We believe that the TMS parameterization does not have the same effect on the
588 Southern Hemisphere as on the Arctic sea ice. In the Arctic, the TMS leads to much
589 thicker sea ice in the central Arctic. By its nature, the TMS parameterization takes
590 momentum from the equatorial region and moves it towards the pole. The excess
591 momentum leads to a cooling of the Polar Regions. Hence the differing effects in the
592 two hemispheres: In the south, the momentum is deposited over the continent and
593 does not overly affect the Southern Ocean sea ice; while in the north, the excess
594 momentum is deposited in the center of the Arctic Ocean, leading to substantial cooling

and thicker sea ice. However, the benefits of TMS to the overall T31x3 model outweigh the detrimental effects on sea ice, hence TMS is applied by default to this configuration.

6. Climate Variability

a. ENSO

The variability of ENSO on decadal to centennial time scales (e.g. Wittenberg 2009) requires us to provide a general circulation model for ENSO research that is fast but realistic, and simulates the full set of relevant processes. In CCSM4 the modification of the convection scheme to account for convective plume dilution and convective momentum transport is a milestone for model development, because it resulted in realistic ENSO periods and amplitudes (Neale et al. 2008). These improvements are realized in the coarse resolution T31x3 as well (Jochum et al. 2009), and the efficiency of this version allows for the rigorous statistical testing of ENSO hypotheses (Stevenson et al. 2010).

A detailed discussion of ENSO in the T31x3 resolution is beyond the scope of this brief overview and the reader is referred to Jochum et al. (2010). The purpose here is merely to demonstrate that the recent release has realistic periods and amplitudes, too. The spectra are based on the NINO3 SST (SST averaged over 150°W-90°W and 5°S-5°N) of the years 201-500 for each of the control simulations, and on the NINO3 SST of the 130

year HadSST reconstruction (Rayner et al. 2006) for the observations (Fig. 17). The T31x3 simulations exhibit a broad spectrum of energy between 2 and 6 years as in the observations. This is true for the FV simulations as well, but the FV2x1 amplitude is excessive compared to observations. Thus, the new convection scheme does lead to realistic periods for all simulations, but does not seem to affect the amplitude of ENSO.

Purely kinematic arguments suggest that the ENSO amplitude has to depend on the zonal as well as vertical temperature gradient along the equator (e.g.; Schopf and Burgman 2006), but nonlinear feedbacks between SST and wind anomalies complicate the matter (e.g.; Gebbie et al. 2007). There are insufficient observations available to constrain the relative contribution of these processes (Capotondi et al. 2006 provides an exhaustive list), but it appears that anticorrelation between the strength of ENSO and of the seasonal cycle is a robust signal across all simulations (Table 1). We see that the relative strength of the seasonal cycle is a good predictor for the strength of ENSO, including observations, but that the mean SST is of little importance. By analyzing equatorial SST before and after the 1976 climate shift, this anticorrelation can actually be observed, and Guilyardi (2006) attributes it to the fact that, because ENSO is a disruption of the seasonal cycle, a weaker seasonal cycle is easier to be disrupted -and vice versa. This suggests that optimizing the simulated ENSO amplitude requires an improved simulation of the seasonal cycle.

636

637 *b. NAM and SAM*

638 Sea level pressure (PSL) and the Northern Annular Mode (NAM) in the T31x3 are
 639 comparable to the FV2x1. In the FV2x1, the strength of the North Atlantic winter low is
 640 too strong whereas in T31x3 it is too weak. In the Southern Hemisphere, the T31x3 has a
 641 slight high bias over the Antarctic continent (not shown).

642 To validate NAM in T31x3, data from the last 26 years (1979-2005) of T31x3_20C are
 643 used to calculate the first empirical orthogonal function (EOF) of winter PSL (December,
 644 January, February, and March). This time period was chosen to match observational
 645 records utilizing consistent and synchronous data across each separate data source. The
 646 principle components timeseries (PC1) are correlated against timeseries of surface
 647 temperature (TS) and precipitation rate (PRECT). Observational data sets are taken from
 648 the Hadley Center (PSL) (Allan and Ansell 2006), NCEP/NCAR Reanalysis (TS) (Kalnay et
 649 al. 1996), and GPCP (PCP) Yin et al. 2004) for years 1979-2008. To evaluate NAM in the
 650 control simulations, data (north of 20°N) was taken from the last 100 years of each
 651 experiment (T31x3_1850 and FV2x1_1850).

652

653 T31x3_20C captures the PSL spatial variability and represents both major centers of
 654 action in the waters north of 60°N and over European continent. The shape and extent
 655 of the North Atlantic center of action, seen in Fig.18, approximate observations

although the low resolution model extends this feature more deeply into North America than exists in the observations. The obvious problem with the NAM, however, is a third center of action in central north Pacific which is significantly larger when compared to observations. This “tri-pole” pathology has existed in all previous versions and resolutions of CCSM (Yeager et al 2006) and CCSM4 is no different.

When analyzing the 1850 control experiments, the north Pacific feature appears to be much stronger in FV2x1_1850 and accounts for the largest variance in EOF1 PSL, (Fig. 19). T31x3 and FV2x1 EOF1 PSL exhibit different yet arguably equivalent errors in both shape and placement of NAM patterns. Correlations of PSL PC1 to TS and PRECT (Fig. 18) show T31x3_20C capturing the key areas of temperature and precipitation anomalies across Europe and the Mediterranean region associated with NAM (Fig 19).

The Southern Annular Mode (SAM) was also computed for the low resolution control run, (not shown). T31x3 PSL variability over the Antarctic continent is much higher than observed. The FV2x1 does a better job at capturing shape and intensity of PSL EOF1 over the Antarctic as well as EOF1 correlation to sea ice extent and surface temperature.

SAM was computed using annual PSL EOF1 across the last 50 years of the control simulations. NCEP records from 1979-2002 show 27% of the variance can be explained by PSL PC1 timeseries while this value for the T31x3_1850 and FV2x1_1850 simulations is 39% and 28%, respectively. Understanding why Antarctic sea ice and Southern Ocean climate compare well to observations while SAM is problematic is a subject for further

study. A detailed analysis of sea level pressure in the context of the TMS parameterization is an obvious place to start, although the SAM problem appears to be more of a function of resolution rather than one with TMS. Spatial patterns of SAM and mean sea level pressure over Antarctica are not substantially different with or without TMS, and in fact, including TMS reduces the mean SLP biases over Antarctica.

7. Climate Sensitivity

The equilibrium climate sensitivity due to a doubling of CO₂ was assessed for the T31x3 model. This is accomplished by extracting implied horizontal and vertical oceanic heat transports and the mixed layer depths from the fully coupled control simulation. These forcing fields are then applied to a slab ocean model (SOM) formulation underneath fully-active sea ice and atmosphere components (Bitz et al. 2011). Simulations were performed at 1850 CO₂ levels and double the 1850 level to assess the change in globally averaged surface temperature due to an instantaneous doubling of CO₂. By this definition, we found the low resolution CCSM4 has a climate sensitivity of 2.9°C which is somewhat higher than its complement in CCSM3 (2.32°C) (Kiehl et al 2006). The higher sensitivity of CCSM4 compared to CCSM3 is consistent across all resolutions of the model. As a detailed discussion of sensitivity and its resolution dependencies is beyond the scope of this paper, readers are encouraged to see Bitz et al. (2011) for an in-depth analysis of CCSM4 sensitivity.

698

699 **8. Model Performance**

700 We have assessed the low resolution CCSM4 performance on three platforms typically
701 used to integrate the model. We have tried a variety of load balancing scenarios using
702 MPI (Message Passing Interface) and OpenMP (Open Multi-Processing) parallelization.
703 The model scales well over a fairly wide range of processor counts (Table 2). The best
704 tested performance is 72 simulation years per actual (wallclock) day value on the
705 National Center for Atmospheric Research's IBM Power6 with 192 processors (pes) and
706 a total cost of 32 pe-hours/model year. By contrast, the FV2x1 model simulates
707 approximately 15 simulation years per (wallclock) day with the same amount of
708 processors. However, it should be noted that the optimal configuration for FV2x1 on
709 the IBM Power6 utilizes 576 processors which produces a throughput of 35 simulated
710 years per (wallclock) day with a total cost of 200 pe-hours/model year. T31x3 is
711 approximately six times less expensive than FV2x1 when running with respective
712 optimal configurations. Other CCSM4-supported machines include Linux clusters as well
713 as Cray XT4's. We can achieve almost 20 years per day on NCAR's Linux cluster (Intel
714 CentOS) with 64 processors, and ~64 years per day on the National Energy Research
715 Scientific Computing Center's (NERSC) Cray XT4 with 420 processors.

716

717 Data volume is another consideration when resources are limited. In its default
718 configuration, the low resolution CCSM4 produces approximately 1.9Gbytes/simulated-

year of data. The intermediate resolution produces ~16.6 Gbytes/simulated-year and the standard resolution produces ~19.7 Gbytes/simulated-year. Of course, data volume can be controlled within the model by limiting model history variables and frequency of output. Due to the wide range of model configurations (resolutions and model components), supported machines, and potential processor configurations, we direct further inquiry on CCSM4 model performance and data volume statistics to the Community Earth System Model website at <http://www.cesm.ucar.edu/models/ccsm4.0>.

9. Discussion and Summary

The low resolution version of CCSM4 can be an alternative to the intermediate version of the model for most applications where cost is an issue. Long equilibrium runs, sensitivity experiments requiring numerous simulations, and model development projects are examples of science problems that require many simulation years. T31x3 is in agreement with both the observational 20th century temperature anomaly record and FV1x1 simulated anomalies. FV2x1 20th century temperature anomalies are higher than both observations and other resolutions. Precipitation patterns for T31x3 across the globe are similar to that of FV2x1 and FV1x1 in that major biases, such as the double ITCZ, exist in all resolutions. Analysis of river transport as a metric to approximate the accuracy of the model water balance, in particular precipitation and river runoff, show the T31x3 model to approximate the FV2x1 in the Pacific basin and perform better in

740 the Atlantic and Indian Ocean basins. The AMOC remains robust in the T31x3 although
741 mixed layer depths remain too shallow in the North Atlantic. Maximum zonal wind
742 stress magnitude for the Southern Hemisphere appears more in line with observational
743 estimates than in the higher resolutions, although the storm track in the low resolution
744 model is displaced equatorward. This equatorial shift in the zonal surface stress in the
745 Southern Hemisphere is a reflection of the Southern Hemisphere jet bias in the
746 atmosphere and may have implications for Southern Ocean studies. The 500 hPa
747 geopotential height is an improvement upon the FV2x1 in the Pacific Northwest,
748 although biases still exist in Arctic. The T31x3 model has a significant cold bias
749 compared to the higher resolutions and observations. Low northward heat transport
750 and cold surface temperatures, particularly in northern Arctic locales, lead to thick and
751 extensive amounts of sea ice. The T31x3 Antarctic sea ice solution, however, is in
752 agreement with observational records, in part, due to improved wind stress.

753

754 Climate variability was also evaluated by analyzing ENSO, NAM, and SAM. T31x3
755 simulates the amplitude and period of ENSO events realistically compared to
756 observations. Although the FV2x1 ENSO yields realistic periods as well, amplitudes are
757 too large. The discrepancy in amplitude between T31x3 and FV2x1, however, is likely
758 due to the implementation of the TMS parameterization in T31 CAM rather than a
759 function of resolution. NAM in T31x3 does not degrade with lower resolution and
760 produces realistic statistics associated with this mode of variability. SAM variability,

761 however, is simulated more realistically with the FV2x1 and does show improvement
762 with higher resolution.

763

764 Aside from the issues stated in this paper, the climate of T31x3 does not significantly
765 degrade from the climate of FV2x1 but is a faster and more economical model. T31x3
766 can be considered a useful tool for experiments and projects that require many
767 simulation hours. It is nearly 5 times faster than FV2x1 when running with the same
768 number of nodes and processors on a supercomputer yet flexible enough to work on a
769 much smaller Linux machine with far less computing power.

770

771

772

773

774

775

776

777

778

779 **Acknowledgements**

780 NCAR and CCSM are sponsored by the National Science Foundation (NSF). We thank all
781 CCSM scientists and software engineers for their hard work in developing and
782 maintaining CCSM4. In particular, we would like to thank the software engineering
783 group for their technical support as well as the CCSM co-chair group for their willingness
784 to spend the time necessary to present the best possible model to the community. We
785 would also like to thank Andy Mai for his efficiency in completing the low resolution 20th
786 century simulation and three anonymous reviewers for their helpful comments. This
787 research was supported by the National Science Foundation; the Office of Science (BER),
788 U. S. Department of Energy (Shields), NSF SGP program (Shields), and NSF OPP 0908675
789 (Bailey). Computing resources were provided by the Climate Simulation Laboratory at
790 NCAR's Computational and Information Systems Laboratory (CISL), sponsored by NSF
791 and other agencies. This research was enabled by CISL compute and storage resources.
792 Bluefire, a 4,064-processor IBM Power6 resource with a peak of 77 TeraFLOPS provided
793 more than 7.5 million computing hours, the GLADE high-speed disk resources provided
794 0.4 PetaBytes of dedicated disk and CISL's 12-PB HPSS archive provided over 1 PetaByte
795 of storage in support of this research project.

796

797

798

799 **References**

- 800 Allan, R. J. and Ansell, T.J., 2006: A new globally complete monthly historical mean sea
801 level pressure data set (HadSLP3): 1850-2004, *J. Climate.*, **19**, 5816-5842..
802
- 803 Bitz, C. M., M. M. Holland, E. C. Hunke, and R. E. Moritz, 2005: Maintenance of the Sea-
804 Ice Edge. *J. Climate*, **18**, 2903-2921.
805
- 806 Bitz, C., K.M. Shell, P.R. Gent, D. Bailey, G. Danabasoglu, K.C. Armour, M.M. Holland, and
807 J.T. Kiehl, 2011: Climate Sensitivity in the Community Climate System Model Version
808 4. *J. Climate*, (in press).
809
- 810 Boville, B. A., 1991: Sensitivity of simulated climate to model resolution., *J. Climate*, **4**,
811 469-485.
812
- 813 Boville, B.A., and P.R. Gent, 1998: The NCAR climate system model, version one. *J.*
814 *Climate*, **11**, 1115-1130.
815
- 816 Brohan, P., J.J. Kennedy, I. Harris, S.F. Tett, and P.D. Jones, 2006: Uncertainty estimates
817 in regional and global observed temperature changes: a new dataset from 1850. *J.*
818 *Geophys. Res.*, **111**, D12106, doi:10.1029/2005JD006548.
819
- 820 Capotondi A., A. Wittenberg, and S. Masina, 2006: Spatial and temporal structure of
821 Tropical Pacific interannual variability in 20th century coupled simulations, *Ocean*
822 *Modelling*, **15**, 274-298, doi:10.1016/j.ocemod.2006.02.004.
823
- 824 Cavalieri, D., C. Parkinson, P. Gloersen, and H.J. Zwally, 1996: Sea ice concentrations
825 from Nimbus-7 SMMR and DMSP SSM/I passive microwave data; updated. National
826 Snow and Ice Data Center, Boulder, CO.
827
- 828 Collins, W.D., C.M. Bitz, M.L. Blackmon, M.L., G.B. Bonan, C.S. Bretherton, J.A. Carton, P.
829 Chan, S.C. Doney, J.J. Hack, T.B. Henderson, J.T. Kiehl, W.G. Large, D.S. McKenna,
830 B.D. Santer, and R.D. Smith, 2006: The Community Climate System Model Version 3
831 (CCSM3), *J. Climate*, **19**, 2122-2161.
832
- 833 Cunningham, S. A., S. G. Alderson, B. A. King, and M. A. Brandon, 2003: Transport and
834 variability of the Atlantic Circumpolar Current in Drake Passage. *J. Geophys. Res.*,
835 **108**, 8084, doi:10.1029/2001JC001147.
836
- 837 Cunningham, S. A., and Co-authors, 2007: Temporal variability of the Atlantic meridional
838 overturning circulation at 26.5°N. *Science*, **317**, 935-938,
839 doi:10.1126/science.1141304.
840

- Dai A., and K.E. Trenberth, (2002): Estimates of freshwater discharge from continents: latitudinal and seasonal variations. *J Hydrometeorol* 3:660-687.
- Danabasoglu, G., 1998: On the wind-driven circulation of the uncoupled and coupled NCAR climate system ocean model. *J. Climate*, **11**, 1442-1454.
- Danabasoglu, G., W.G. Large, and B.P. Briegleb, 2010: Climate impacts of parameterized Nordic Sea overflows. *J. Geophys. Res.*, **115**, C11005, doi:10.1029/2010JC006243.
- Danabasoglu, G., S. Bates, B. P. Briegleb, S. R. Jayne, M. Jochum, W. G. Large, S. Peacock, and S. G. Yeager, 2011: The CCSM4 ocean component. *J. Climate* (accepted).
- ETOPO2v2, 2006: 2-minute gridded global relief data. U.S. Department of Commerce, National Oceanic and Atmospheric Administration, National Geophysical Data Center. [Available online at <http://www.ngdc.noaa.gov/mgg/fliers/06mgg01.html>].
- Gebbie, G., I. Eisenman, A. Wittenberg, and E. Tziperman, 2007: Modulation of Westerly Wind Bursts by Sea Surface Temperature: A Semistochastic Feedback for ENSO. *Journal of Atmospheric Sciences*, **64**, 3281-3295.
- Gent P.R., S.G. Yeager, R.B. Neale, S. Levis, and D. A. Bailey, D.A., 2010: Improvements in a half degree atmosphere/land version of the CCSM. *Climate Dynamics*, **34**, 819-833, doi: 10.1007/s00382-009-0614-8.
- Gent, P.R., Danabasoglu, G., Donner, L. J., Holland, M.M., Hunke, E.C., Jayne, S.R., Lawrence, D.M., Neale, R.B., Rasch, P.J., Vertenstein, M., Worley, P.H., Yang, Z.-L., Zhang, M., 2011: The Community Climate System Model version4. *J. Climate*, (in press).
- Guilyardi, E., 2006: El Nino-mean state-seasonal cycle interactions in a multi-model ensemble. *Climate Dynamics*, **26**, 329-348, doi: 10.1007/s00382-005-0084-6.
- Hack, J., Caron, J., Danabasoglu, G., Oleson, K., Bitz, C., Truesdale, J.E., 2006: CCSM-CAM3 climate simulation sensitivity to changes in horizontal resolution. *J. Climate*, **19**, 2267-2289.
- Holland, M. M. and M. N. Raphael, 2006: Twentieth century simulation of the southern hemisphere climate in coupled models. Part II: sea ice conditions and variability., *Clim. Dyn*, **26**, 229-245.
- Holland, M.M., D.A. Bailey, B.P. Briegleb, B. Light, and E. Hunke, 2011: Improved sea ice shortwave radiation physics in CCSM4: The impact of melt ponds and black carbon. *J. Climate*, (submitted).

- Hunke, E.C. and W. H. Lipscomb, 2008: CICE: The Los Alamos sea ice model user's manual, version 4. Los Alamos National Laboratory Tech. Report LA-CC-06-012.
- Hurrell, J. W., J. J. Hack, D. Shea, J. M. Caron, and J. Rosinski, 2008: A new sea surface temperature and sea ice boundary dataset for the Community Atmosphere Model. *J. Climate*, **21**, 5145-5153, doi:10.1175/2008JCLI2292.1.
- Jablonowski, C. and D. L. Williamson, 2006: A Baroclinic Instability Test Case for Atmospheric Model Dynamical Cores, *QJRM*, **132**, 2943-2976.
- Jahn, A., D.A. Bailey, C.M. Bitz, M.M. Holland, E.C. Hunke, J. E. Kay, W. H. Lipscomb, J.A. Maslanik, D. Pollak, K. Sterling, J. Ströve., 2011: Late 20th Century Simulation of Arctic Sea Ice and Ocean Properties in the CCSM4. *J. Climate*, (accepted).
- Jochum, M., G. Danabasoglu, M. Holland, Y.-O. Kwon, and W.G. Large, 2008: Ocean viscosity and climate. *J. Geophys. Res.*, **113**, C06017, doi:10.1029/2007JC004515.
- Jochum, M., B. Fox-Kemper, P.H. Molnar, and C. Shields, 2009: Differences in the Indonesian seaway in a coupled climate model and their relevance to Pliocene climate and El Nino. *Paleoceanography*, **24**, PA1212, doi:10.1029/2008PA001678.
- Jochum, M., S. Yeager, K. Lindsay, K. Moore, and R. Murtugudde, 2010: Quantification of the Feedback between Phytoplankton and ENSO in the Community Climate System Model. *J. Climate*, **23**, 2916-2925.
- Johns, W. E., and Co-authors, 2011: Continuous, array-based estimates of Atlantic Ocean heat transport at 26.5°N. , *J. Climate* (submitted).
- Johnson, G., B. Sloyan, W. Kessler, and K. McTaggart, 2002: Direct measurements of upper ocean currents and water properties across the tropical Pacific during the 1990s. *Progress in Oceanography*, **52**, 31-61.
- Kalnay E., M. Kanamitsu, R. Kistler, W. Collins, D. Deaven, L. Gandin, M. Iredell, S. Saha, G. White, J. Woollen, Y. Zhu, A. Leetmaa, R. Reynolds, M. Chelliah, W. Ebisuzaki, W. Higgins, J. Janowiak, K. C. Mo, C. Ropelewski, J. Wang, R. Jenne, D. Joseph, 1996: The NCEP/NCAR 40-year reanalysis project, *Bull. Amer. Meteor. Soc.*, **77**, 437-470.
- Kiehl, J.T., C.A. Shields, J.J. Hack, and W.D. Collins, W.D., 2006: The Climate Sensitivity of the Community Climate System Model Version 3 (CCSM3). *J. Climate*, **19**, 2584-2596.
- Klinker, E., and P.D. Sardeshmukh, 1992: The Diagnosis of Mechanical Dissipation in the Atmosphere from Large-Scale Balance Requirements. *Journal of Atmospheric Sciences*, **49**, 608-627.

- 929 Large, W. G., and S. G. Yeager, 2009: The global climatology of an interannually varying
 930 air-sea flux data set. *Clim. Dyn.*, **33**, 341-364, doi:10.1007/s00382-008-0441-3.
 931
- 932 Lawrence, D.M., K.W. Oleson, M.G. Flanner, C.G. Fletcher, P.J. Lawrence, S. Levis, S.C.
 933 Swenson, and G.B. Bonan, 2011: The CCMS4 land simulations, 1850-2005:
 934 Assessment of surface climate and new capabilities. *J. Climate*, (accepted).
 935
- 936 Levitus, S., T. Boyer, M. Concright, D. Johnson, T. O'Brien, J. Antonov, C. Stephens, and R.
 937 Garfield, 1998: World Ocean Database 1998, volume I: Introduction.
 938 U.S.Government Printing Office, Washington, D.C., NOAA Atlas NESDIS 18, 346pp.
 939
- 940 Lin, S. J., 2004: A "Vertically Lagrangian" finite-volume dynamical core for global
 941 models. *Mon. Wea. Rev.*, **132**, 2293-2307.
 942
- 943 Matsuura, K., and C.J. Willmott, 2009: Terrestrial Air Temperature: 1900-2008 Gridded
 944 Monthly Time Series, Version 2.01. Available online at
 945 <http://climate.geog.udel.edu/~climate>.
 946
- 947 Milton, S.F., and C.A. Wilson, 1996: The Impact of Parameterized Subgrid-Scale
 948 Orographic Forcing of Systematic Errors in a Global NWP Model. *Monthly Weather*
 949 *Review*, **124**, 2023-2045.
 950
- 951 Neale, R.B., J.H. Richter, and M. Jochum, 2008: The impact of convection on ENSO: From
 952 a delayed oscillator to a series of events. *J. Climate*, **21**, 5904-5924.
 953
- 954 Neale, R.B., J. Richter, S. Park, P.H. Lauritzen, S.J. Vavrus, P.J. Rasch, and M. Zhang, 2011:
 955 The mean climate of the Community Atmosphere Model version 4 (CAM4) in forced
 956 SST and fully coupled experiments. *J. Climate*, (submitted).
 957
- 958 Otto-Bliesner, B.L., E.C. Brady, and C.A. Shields, 2002: Late Cretaceous ocean: Coupled
 959 simulations with the National Center for Atmospheric Research climate system
 960 model. *J. Geophys Res.*, **107**, 1-14.
 961
- 962 Rayner, N.A., P. Brohan, D.E. Parker, C.K. Folland, J.J. Kennedy, M. Vanicek, T. Ansell and
 963 S.F.B. Tett 2006: Improved analyses of changes and uncertainties in sea surface
 964 temperature measured in situ since the mid-nineteenth century: the HadSST2 data
 965 set. *Journal of Climate*. **19**(3), pp. 446-469.
 966
- 967
- 968 Schopf, P. S., and R. J. Burgman, 2006: A simple mechanism for ENSO
 969 residuals and asymmetry, *J. Climate*, **19**, 3167-3179.
 970
- 971 Smith, R., P. Jones, B. Briegleb, F. Bryan, G. Danabasoglu, J. Dennis, J. Dukowicz, C. Eden,
 972 B. Fox-Kemper, P. Gent, M. Hecht, S. Jayne, M. Jochum, W. Large, K. Lindsay, M.

- Maltrud, N. Norton, S. Peacock, M. Vertenstein, and S. Yeager, 2010: The Parallel Ocean Program (POP) reference manual, Ocean component of the Community Climate System Model (CCSM). LANL Tech. Report, LAUR-10-01853, 141 pp.
- Steele, M., R. Morley, and W. Ermold, 2001: PHC: A global ocean hydrography with a high quality Arctic Ocean. *J. Climate*, **14**, 2079-2087.
- Stevenson, S., B. Fox-Kemper, M. Jochum, Rajagopalan, S. Yeager, 2010: ENSO Model Validation Using Wavelet Probability Analysis. *J. Climate*, **23**, 5540-5547, doi: 10.1175/2010JCLI3609.1.
- Uttal, T., et al, 2002: Surface Heat Budget of the Arctic Ocean. *BAMS*, **83**, 255-276.
- Williamson, D.L., J.T. Kiehl, and J.J. Hack, 1995: Climate sensitivity of the NCAR Community Climate System Model (CCM2) to horizontal resolution. *Climate Dynamics*, **11**, 377-397.
- Wittenberg, A.T., 2009: Are historical records sufficient to constrain ENSO simulations? *Geophysical Research Letters*, **36**, L12702, doi:10.1029/2009GL038710.
- Yeager, S.G., C.A. Shields, W.G. Large, and J.J. Hack, 2006: The Low-Resolution CCSM3. *J. Climate*, **19**, 2545-2566.
- Yin, X., A. Gruber, and P. Arkin, 2004: Comparison of CPCP and CMAP merged gauge-satellite monthly precipitation products for the period 1970-2001., *J. Hydrometeor*, **5**, 1207-1222.

1006 **List of Figures and Tables**

1007 **Fig1.** Annual-mean time series of a) global volume-mean potential temperature, b)
 1008 global volume-mean salinity, and c) Atlantic meridional overturning circulation (AMOC)
 1009 maximum transport for T31x3_1850. AMOC maximum is searched for below 500-m
 1010 depth and between 30o-60oN and it includes the mean flow and parameterized eddy
 1011 contributions.

1012

1013 **Fig2.** Model SST differences ($^{\circ}\text{C}$) from the Hurrell et al. (2008) observational data for a)
 1014 FV1x1_1850, b) FV2x1_1850, and c) T31x3_1850. The 1870-1899 time-mean SST is
 1015 used for observations. The mean and root-mean-square (rms) differences from
 1016 observations are also given.

1017

1018 **Fig3.** Zonal-mean zonal wind stress. LY represents an estimate based on the Large and
 1019 Yeager (2009) dataset.

1020

1021 **Fig4.** Annually average precipitation rate (mm/day) for a) FV1x1_1850, b) FV2x1_1850,
 1022 and c) T31x3_1850.

1023

1024 **Fig5.** Simulated and observed annual discharge from rivers to the ocean shown as a
 1025 cumulative amount from 60°S to 90°N (km³). Discharge to (a) all oceans, (b) the Atlantic,
 1026 (c) the Indian, (d) the Pacific, and (e) the Arctic Ocean.

1027

1028 **Fig6.** Northern Hemisphere JFM (winter) sea ice fraction (%) (upper panels) for
 1029 T31x3_1850, FV2x1_1850, and FV1x1_1850. Southern Hemisphere JFM (summer) sea
 1030 ice fraction (%) (lower panels) for T31x3_1850, FV2x1_1850, FV1x1_1850. SSM/I
 1031 observations for sea ice 10% concentration are shown with heavy black line for
 1032 reference.

1033

1034 **Fig7.** Annual mean timeseries of globally-averaged surface temperature anomaly from
 1035 HadCRUT3v data (Brohan et al., 2006). FV1x1 is an ensemble mean, FV2x1 and T31x3
 1036 are single realizations. Anomalies are computed relative to the mean of the first 20
 1037 years of each timeseries.

1038

1039 **Fig8.** Annually averaged surface air temperature zonal average differences. Dashed line
 1040 shows surface air temperature over land for T31x3_20C minus observations.
 1041 Observations are derived from Matsuura and Willmott (2009) air temperature time
 1042 series. Climatology was computed using years 1950-1999. Solid line shows surface air

1043 temperature globally for T31x3_1850 minus FV2x1_1850. The zero line is marked for
 1044 reference.

1045

1046 **Fig9.** Annually averaged precipitation difference for T31x3_2000 from GPCP
 1047 observations (mm/day).

1048

1049 **Fig10.** Annually averaged zonal mean air temperature ($^{\circ}\text{C}$) with height for a) T31x3_20C
 1050 b) NCEP Reanalysis, c) their difference. Contour intervals for a) and b) are every 5
 1051 degrees from -85°C through -50°C with all subsequent contours every 10°C . Contour
 1052 intervals for c) are (-9, -7, -5, -4, -3, -2, -1, 0, 1, 2, 3, 4, 5, 7, 9). Solid lines are
 1053 positive values and dashed lines are negative values.

1054

1055 **Fig11.** Annually averaged mean zonal wind (ms^{-1}) with height for a) T31x3_20C b) NCEP
 1056 Reanalysis, and c) their difference. Contour intervals for a) and b) are every 5ms^{-1}
 1057 from -20ms^{-1} to 30ms^{-1} with all subsequent contours 10ms^{-1} . Contour intervals for c)
 1058 are (-18, -15, -12, -9, -6, -3, 1, 0, 1, 3, 6, 9, 12, 15, 18). Solid lines are positive values
 1059 and dashed lines are negative values.

1060

1061 **Fig12.** Annually averaged 500 hPa Geopotential Height (hectometers) for a)
 1062 T31x3_20C, b) NCEP Reanalysis, c) difference. Contour intervals for a) and b) are every
 1063 0.5 hectometers. Contour intervals for c) are (-1, -0.8, -0.6, -0.4, -0.3, -0.2, -0.1, 0, 0.1,
 1064 0.2, 0.3, 0.4, 0.6, 0.8, 1) hectometers.

1065

1066 **Fig13.** Sea surface a) temperature (SST, °C) and b) salinity (SSS, psu) T31x3_20C minus
 1067 observations difference distributions. For temperature and salinity, the Hurrell et al.
 1068 (2008) and PHC2 datasets are used, respectively.

1069

1070 **Fig 14.** Meridional overturning circulation (Sv) for a) global and b) Atlantic Oceans from
 1071 T31x3_20C. The plots represent the total overturning circulation that include the
 1072 Eulerian-mean and parameterized mesoscale and submesoscale contributions. The
 1073 positive and negative (shaded regions) contours denote clockwise and counter-
 1074 clockwise circulations, respectively. The contour interval is 4 Sv.

1075

1076 **Fig 15.** a) Global and b) Atlantic Ocean northward heat transports. The global transports
 1077 are the total transports and include the parameterized mesoscale, submesoscale, and
 1078 diffusive contributions as well as the Eulerian-mean component. The Atlantic Ocean
 1079 transports exclude the diffusive component. The dotted line denoted by LY represents
 1080 implied time-mean transport calculated by Large and Yeager (2009) with shading

1081 showing the implied transport range in individual years. The triangle with the error bar
 1082 is an estimate based on the RAPID data from Johns et al. (2011).

1083

1084 **Fig 16.** Northern Hemisphere JFM (winter) sea ice fraction (%) (upper panels) for
 1085 T31x3_20C and FV1x1_20C. Southern Hemisphere JFM (summer) sea ice fraction
 1086 (middle panels) (%) for T31x3_20C and FV1x1_20C. Northern Hemisphere JFM (winter)
 1087 sea ice thickness (m) (lower panels) for T31x3_20C and FV1x1_20C. SSM/I observations
 1088 for sea ice (10% concentration) are shown with heavy black line for reference.

1089

1090 **Fig 17.** Power spectrum for NINO3 SST anomalies for HadSST(black), T311850 (blue),
 1091 T312000(red), FV21850(green), and FV11850(purple). The area under a line, when
 1092 integrated across all periods, yields the total variance.

1093

1094 **Fig 18.** NAM analysis for T31x3_20C (lower panels) versus observations (upper panels).
 1095 Winter (DJFM) PSL EOF1 (left) and correlations to surface temperature and precipitation
 1096 anomaly timeseries (center and right). Observations include the Hadley Center mean
 1097 sea level pressure dataset, NCEP mean monthly air temperature Reanalysis, and GPCP
 1098 precipitation and all use years 1979-2008. Model data matches observational record
 1099 for years 1979-2005. Correlations are plotted at the 95% significance level.

1100

1101 **Fig19.** NAM analysis for T31x3_1850 (lower panels) versus FV2x1_1850 (upper panels).
 1102 Winter (DJFM) PSL EOF1 (left) and correlations to surface temperature and precipitation
 1103 anomaly timeseries (center and right). Model data uses the last 100 years of timeseries
 1104 in simulation. Correlations are plotted at the 95% significance level.

1105

1106 **Table 1.** NINO3 mean SST, and *std* of the seasonal cycle and the interannual variability.

1107

1108 **Table 2.** Low resolution (T31x3) CCSM4 performance on three typical platforms: an IBM
 1109 Power 6; a Cray XT4; and a small Linux cluster. Top performance for each machine is
 1110 highlighted in bold text. **FV2x1 and FV1x1 comparison figures are shown in italics. Note*
 1111 *that T31x3 is not optimized for 512 or 576 pes.*

1112

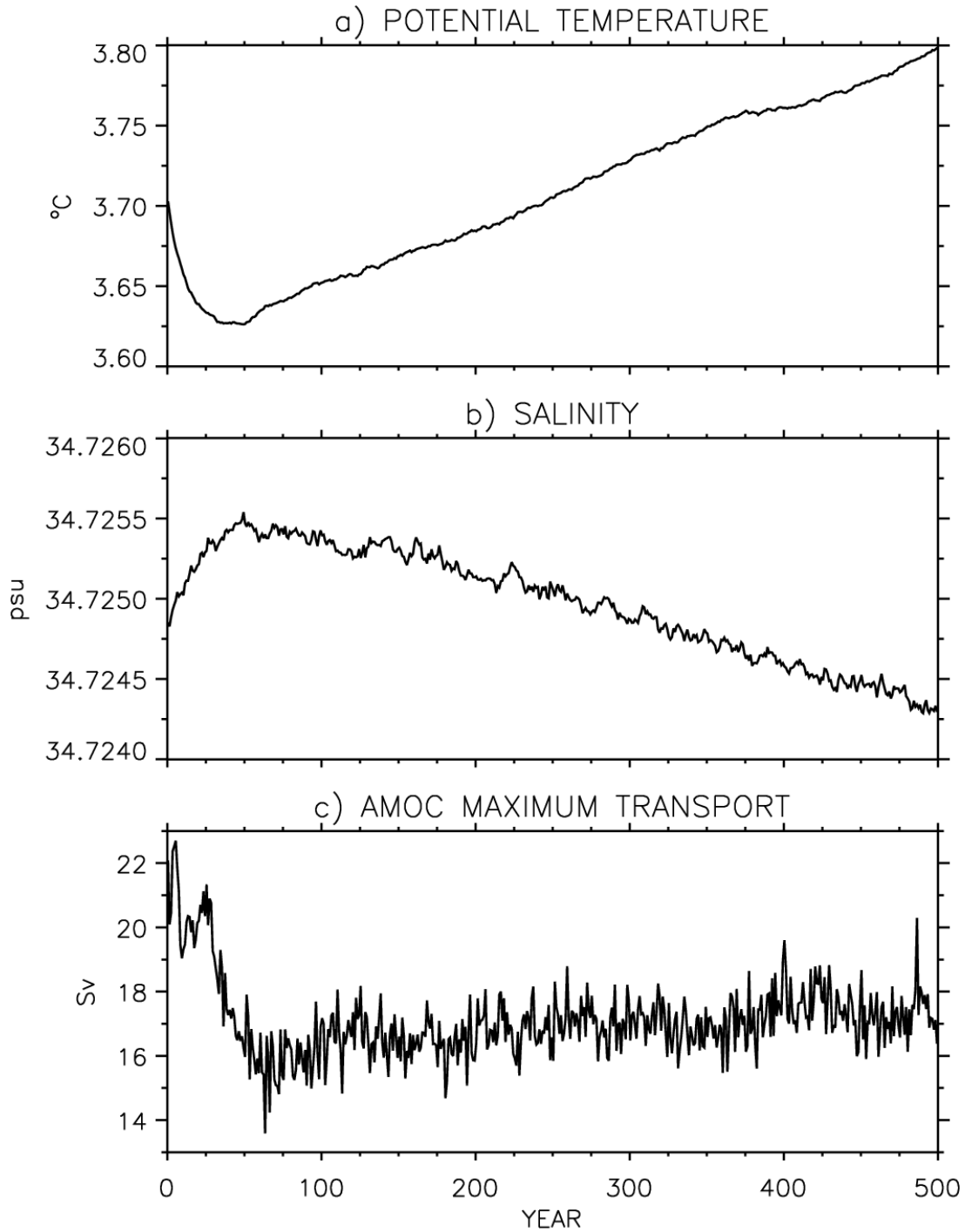


Figure 1. Annual-mean time series of a) global volume-mean potential temperature, b) global volume-mean salinity, and c) Atlantic meridional overturning circulation (AMOC) maximum transport for T31x3_1850. AMOC maximum is searched for below 500-m depth and between 30°-60°N and it includes the mean flow and parameterized eddy contributions.

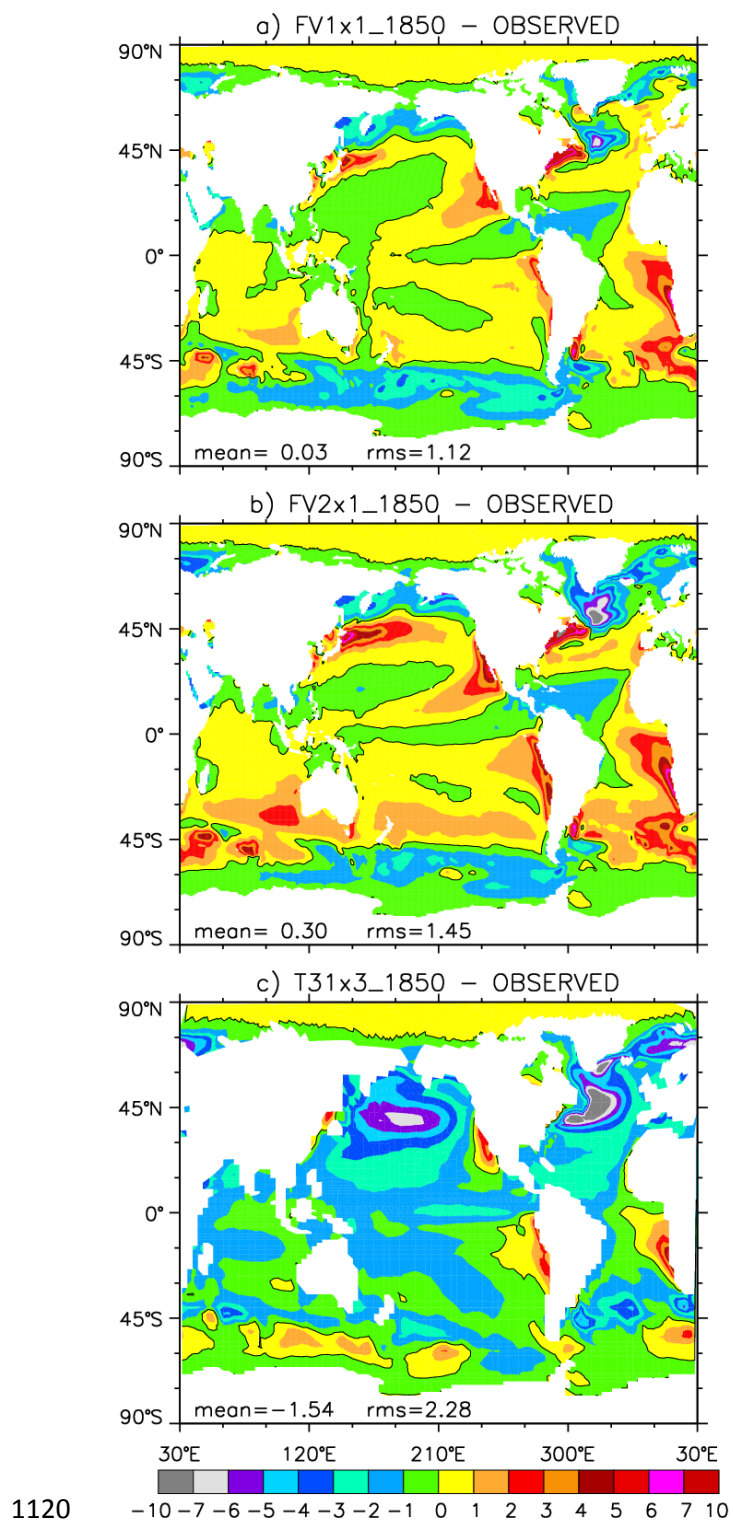
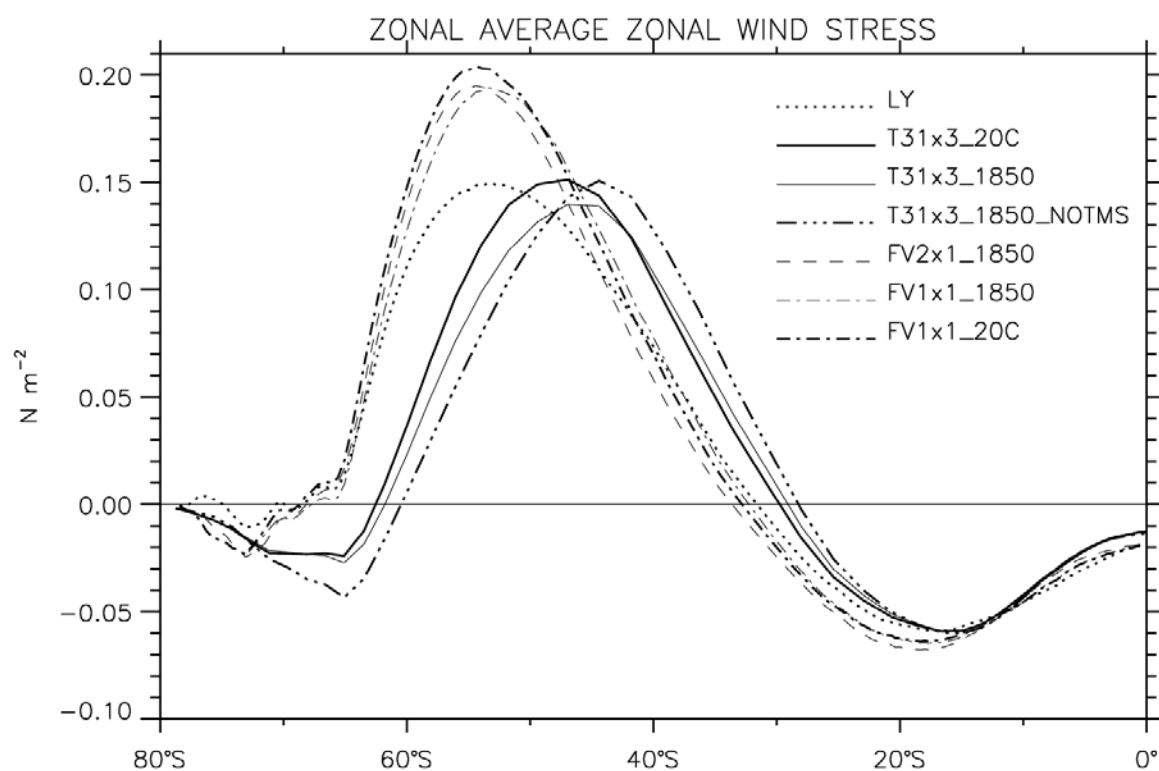


Figure 2. Model SST differences ($^{\circ}\text{C}$) from the Hurrell et al. (2008) observational data for
a) FV1x1_1850, b) FV2x1_1850, and c) T31x3_1850. The 1870-1899 time-mean SST
is used for observations. The mean and root-mean-square (rms) differences from
observations are also given.

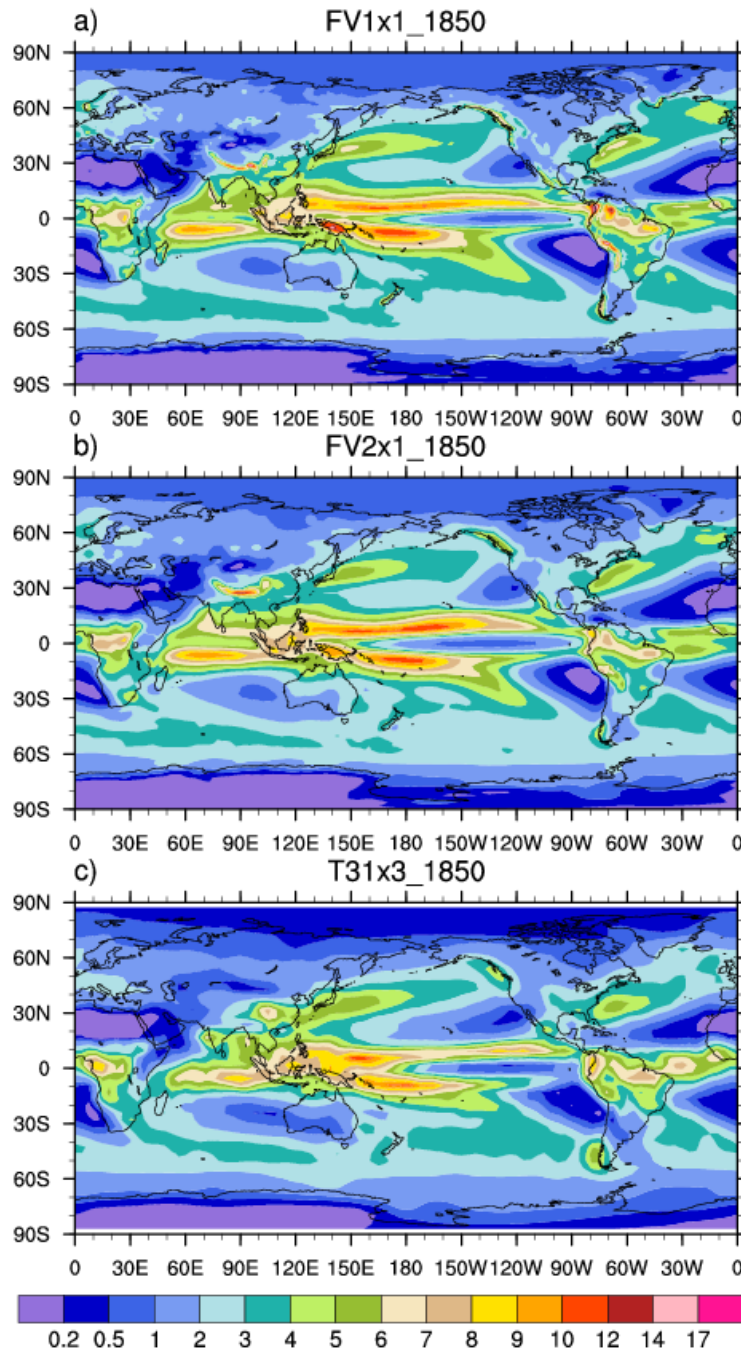
1125



1126

1127 Figure 3. Zonal-mean zonal wind stress. LY represents an estimate based on the Large
 1128 and Yeager (2009) dataset.
 1129

1130

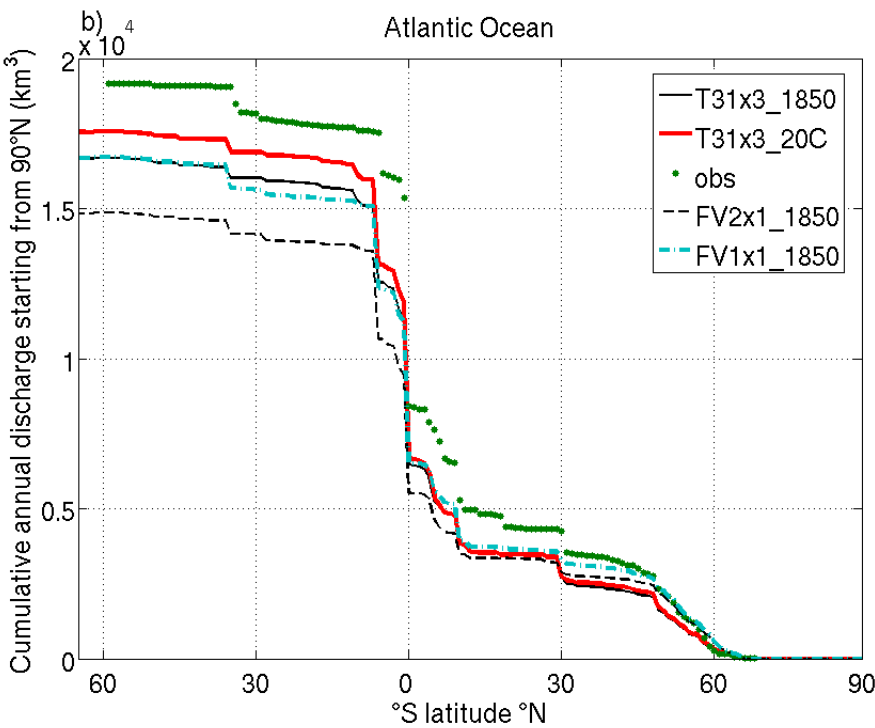
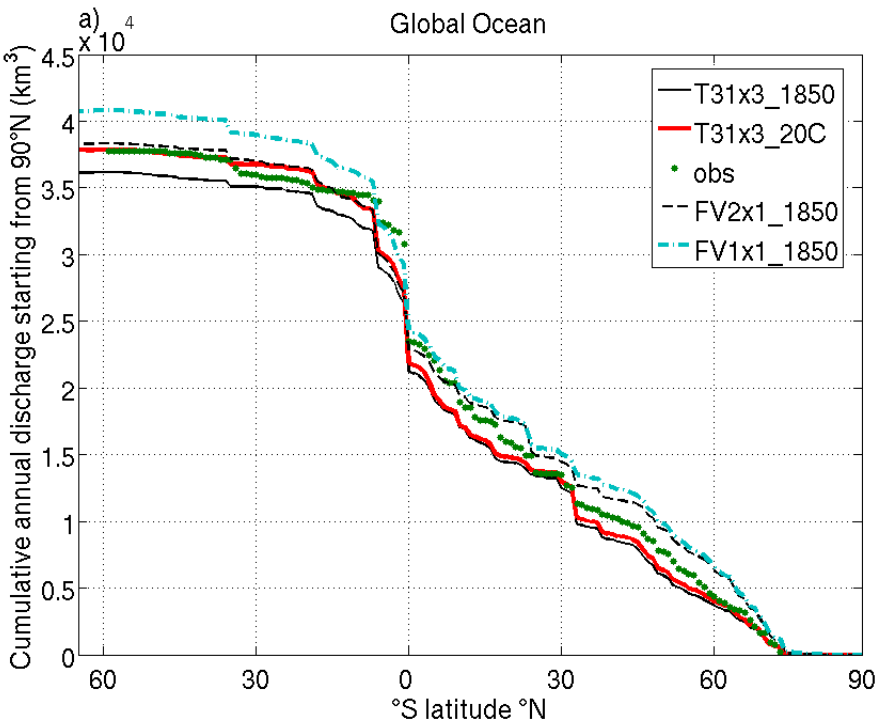


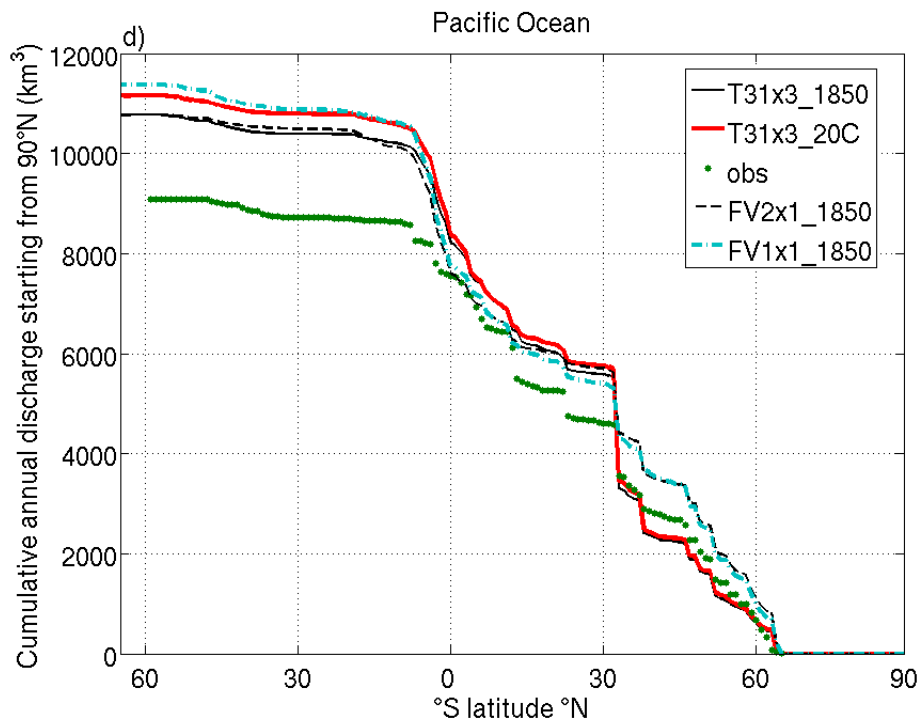
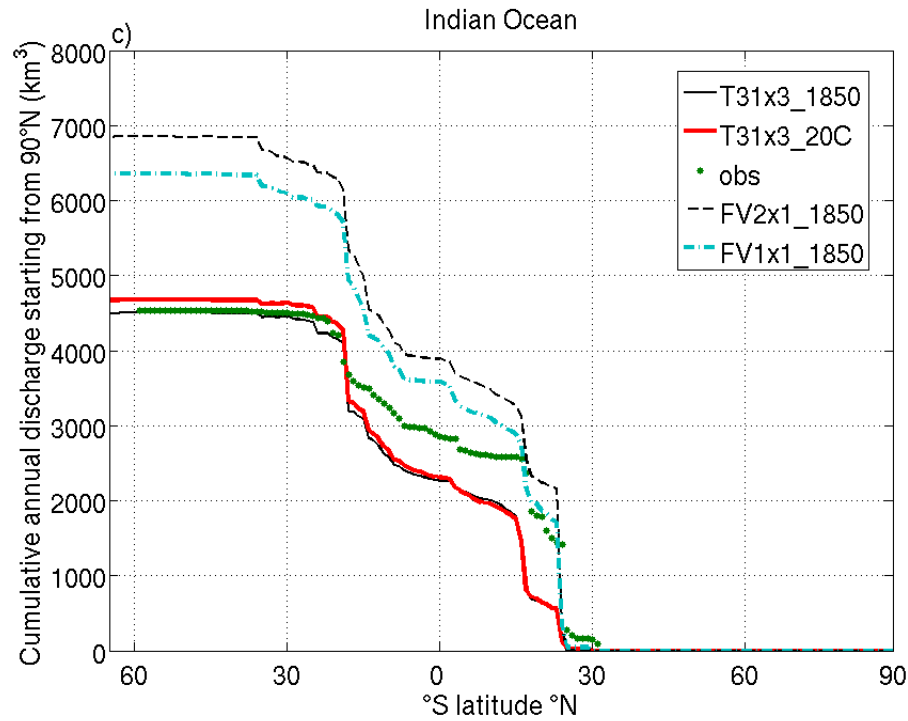
1131

1132 Figure 4. Annually average precipitation rate (mm/day) for a) FV1x1_1850, b)
 1133 FV2x1_1850, and c) T31x3_1850.

1134

1135





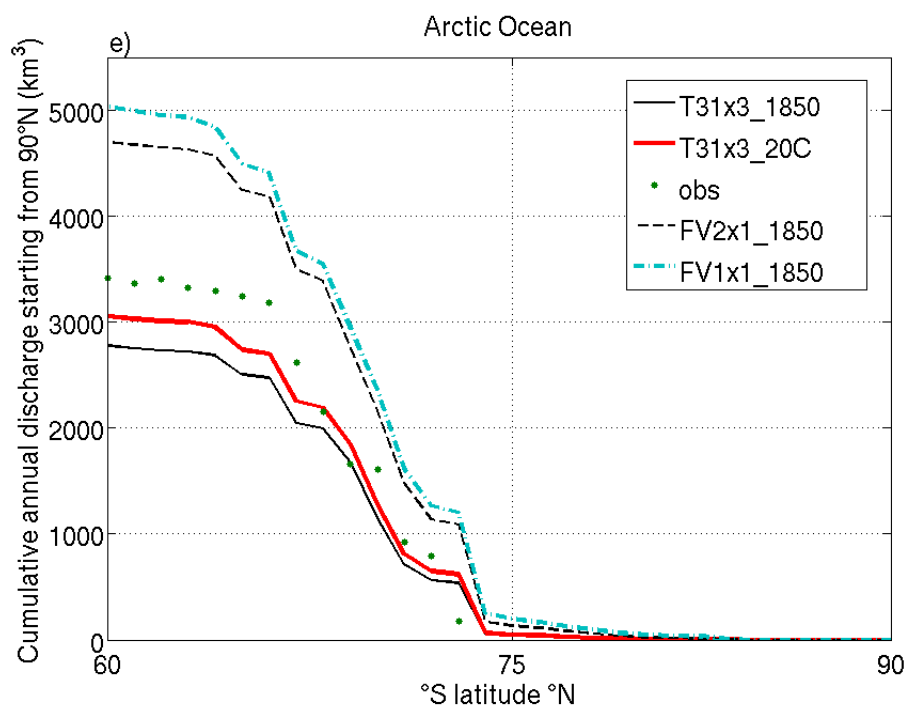


Figure 5. Simulated and observed annual discharge from rivers to the ocean shown as a cumulative amount from 60°S to 90°N (km^3). Discharge to (a) all oceans, (b) the Atlantic, (c) the Indian, (d) the Pacific, and (e) the Arctic Ocean.

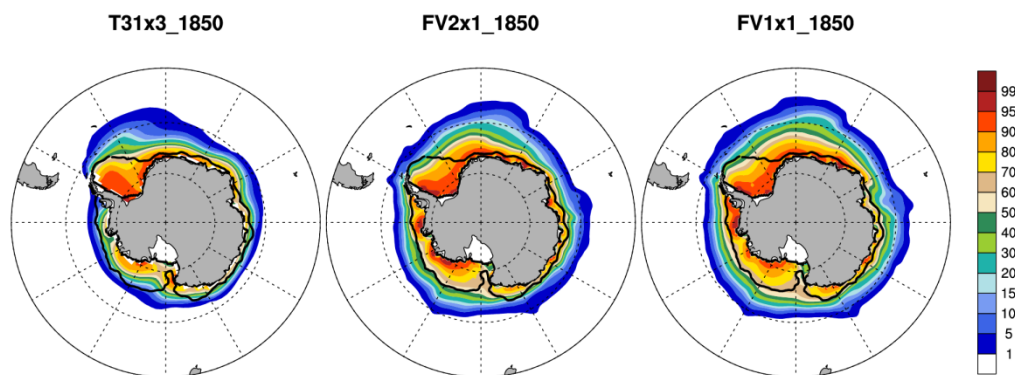
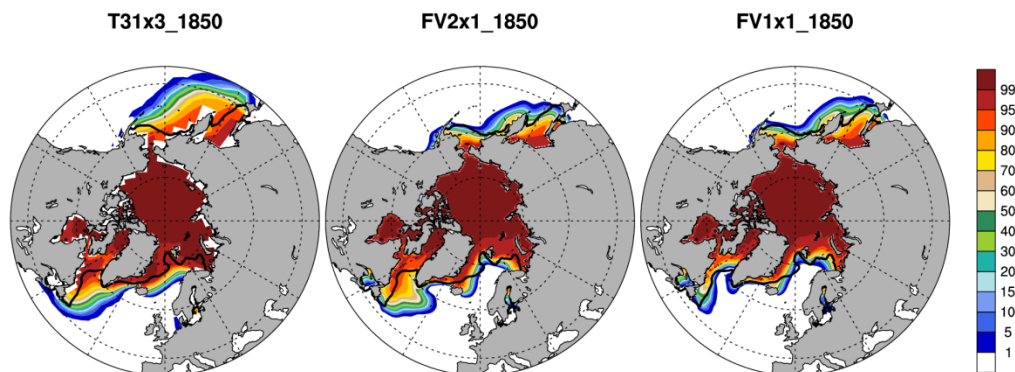
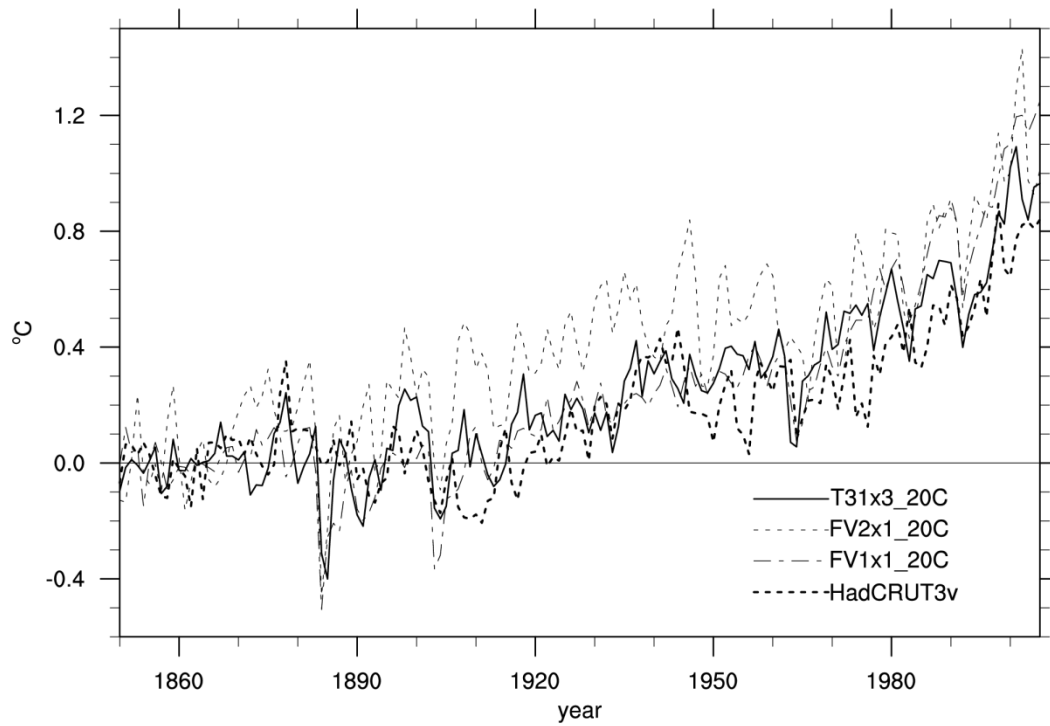


Figure 6. Northern Hemisphere JFM (winter) sea ice fraction (%) (upper panels) for T31x3_1850, FV2x1_1850, and FV1x1_1850. Southern Hemisphere JFM (summer) sea ice fraction (%) (lower panels) for T31x3_1850, FV2x1_1850, and FV1x1_1850. SSM/I observations for sea ice 10% concentration are shown with heavy black line for reference.



1181

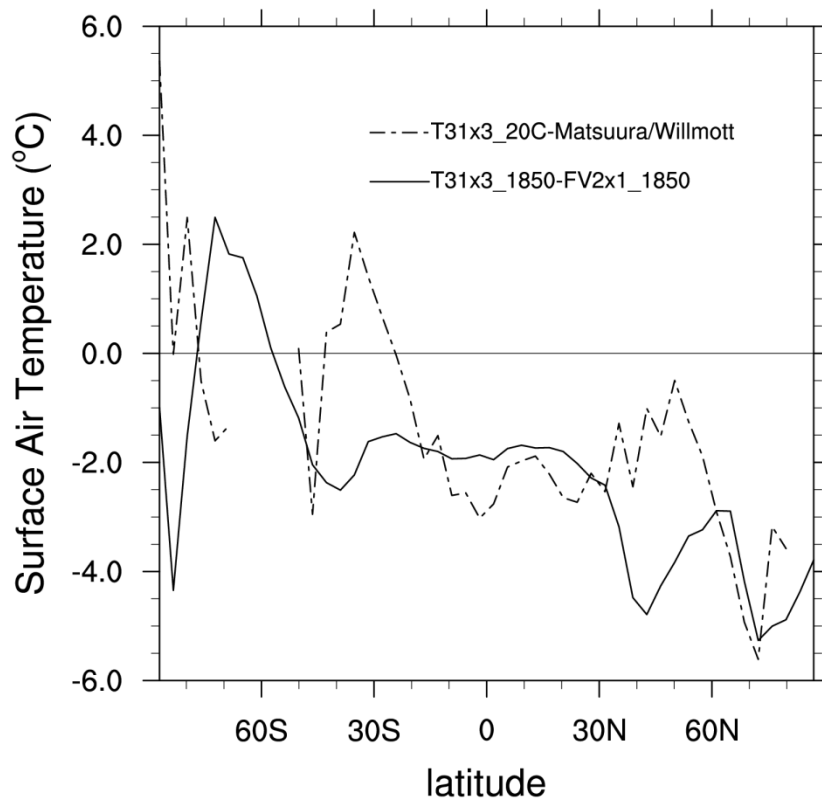
1182 Figure 7. Annual mean timeseries of globally-averaged surface temperature anomaly
 1183 from HadCRUT3v data (Brohan et al., 2006). FV1x1 is an ensemble mean, FV2x1 and
 1184 T31x3 are single realizations. Anomalies are computed relative to the mean of the
 1185 first 20 years of each timeseries.

1186

1187

1188

1189

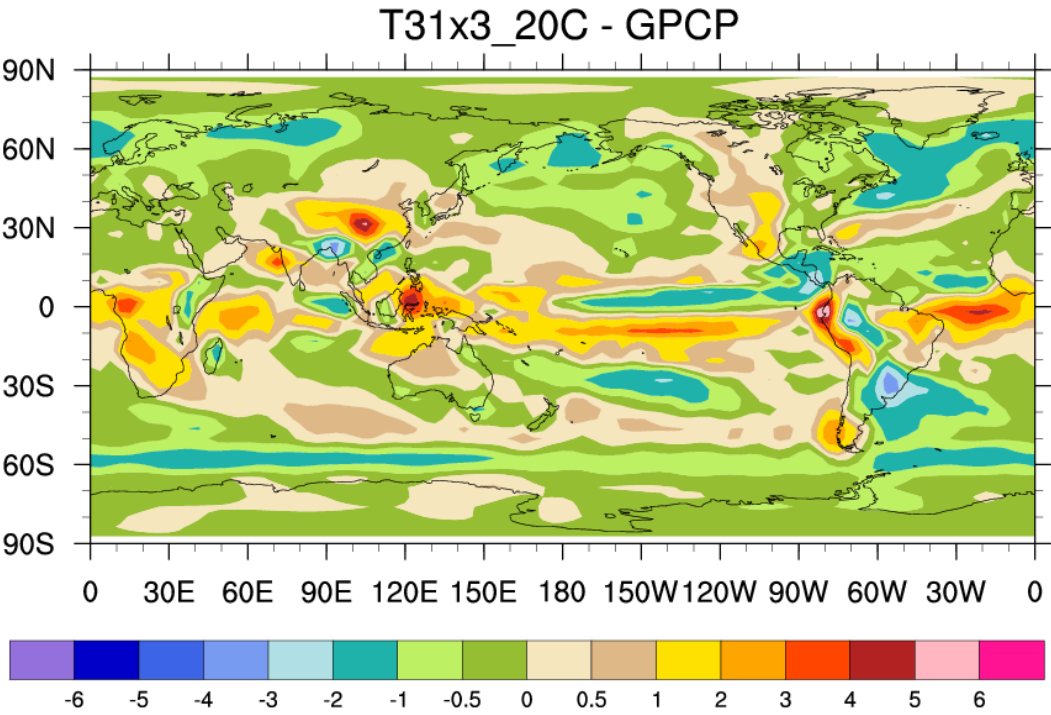


1190

1191 Figure 8. Annually averaged surface air temperature zonal average differences. Dashed
 1192 line shows surface air temperature over land for T31x3_20C minus observations.
 1193 Observations are derived from Matsuura and Willmott (2009) air temperature time
 1194 series. Climatology was computed using years 1950-1999. Solid line shows surface
 1195 air temperature globally for T31x3_1850 minus FV2x1_1850. The zero line is marked
 1196 for reference.

1197

1198



1199

1200 Figure 9. Annually averaged precipitation difference for T31x3_20C from GPCP
1201 observations (mm/day).

1202

1203

1204

1205

1206

1207

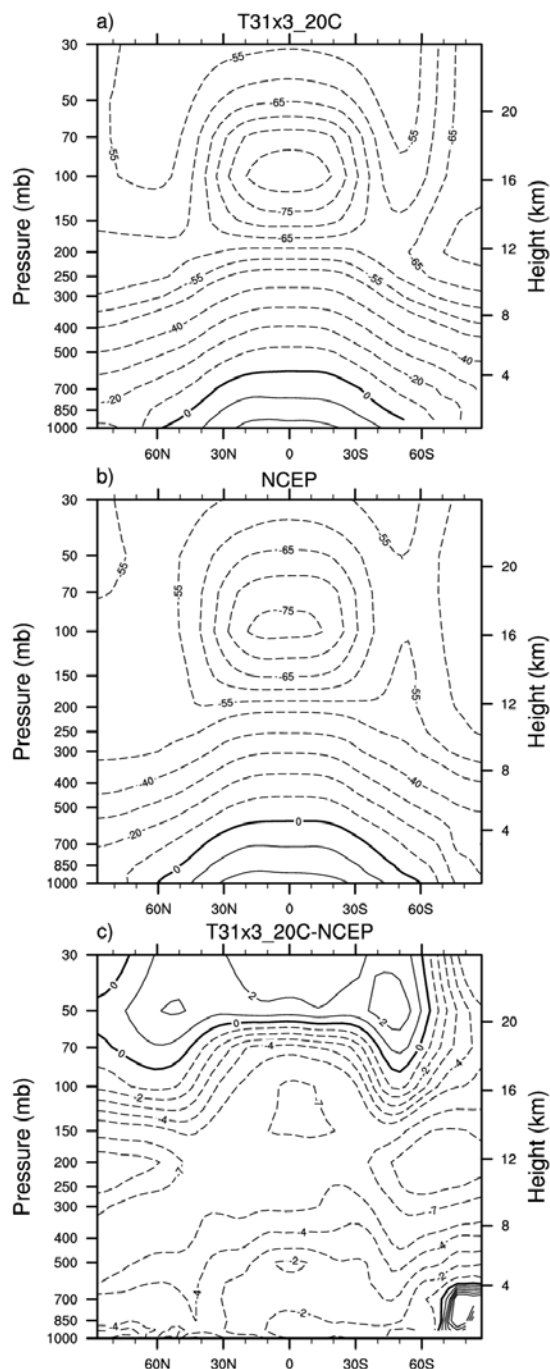


Figure 10. Annually averaged zonal mean air temperature ($^{\circ}\text{C}$) with height for a) T31x3_20C b) NCEP Reanalysis, c) their difference. Contour intervals for a) and b) are every 5 degrees from -85°C through -50°C with all subsequent contours every 10°C . Contour intervals for c) are $(-9, -7, -5, -4, -3, -2, -1, 0, 1, 2, 3, 4, 5, 7, 9)$. Solid lines are positive values and dashed lines are negative values.

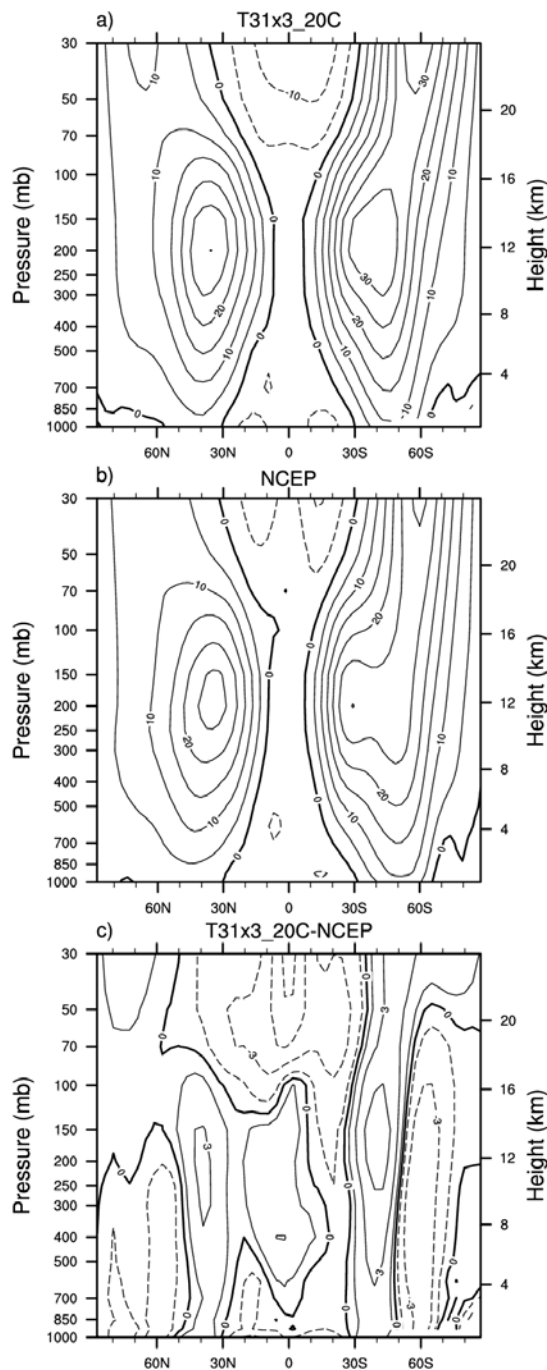


Figure 11. Annually averaged mean zonal wind (ms⁻¹) with height for a) T31x3_20C b) NCEP Reanalysis, and c) their difference. Contour intervals for a) and b) are every 5ms⁻¹ from -20ms⁻¹ to 30 ms⁻¹ with all subsequent contours 10ms⁻¹. Contour intervals for c) are (-18, -15, -12, -9, -6, -3, 1, 0, 1, 3, 6, 9, 12, 15, 18). Solid lines are positive values and dashed lines are negative values.

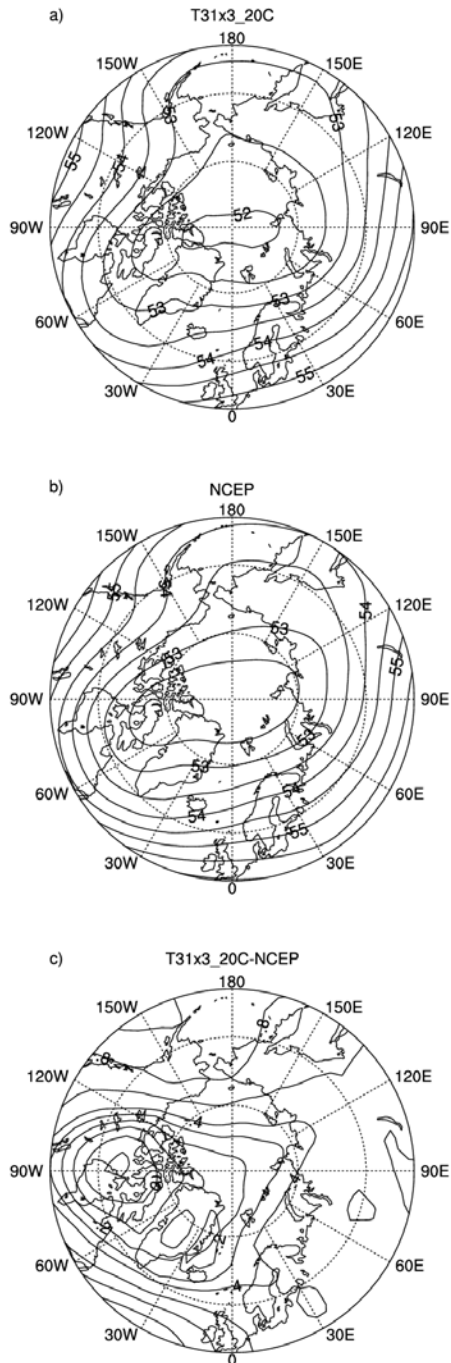


Figure 12. Annually averaged 500 hPa Geopotential Height (hectometers) for a) T31x3_20C, b) NCEP Reanalysis, c) difference. Contour intervals for a) and b) are every 0.5 hectometers. Contour intervals for c) are (-1, -0.8, -0.6, -0.4, -0.3, -0.2, -0.1, 0, 0.1, 0.2, 0.3, 0.4, 0.6, 0.8, 1) hectometers.

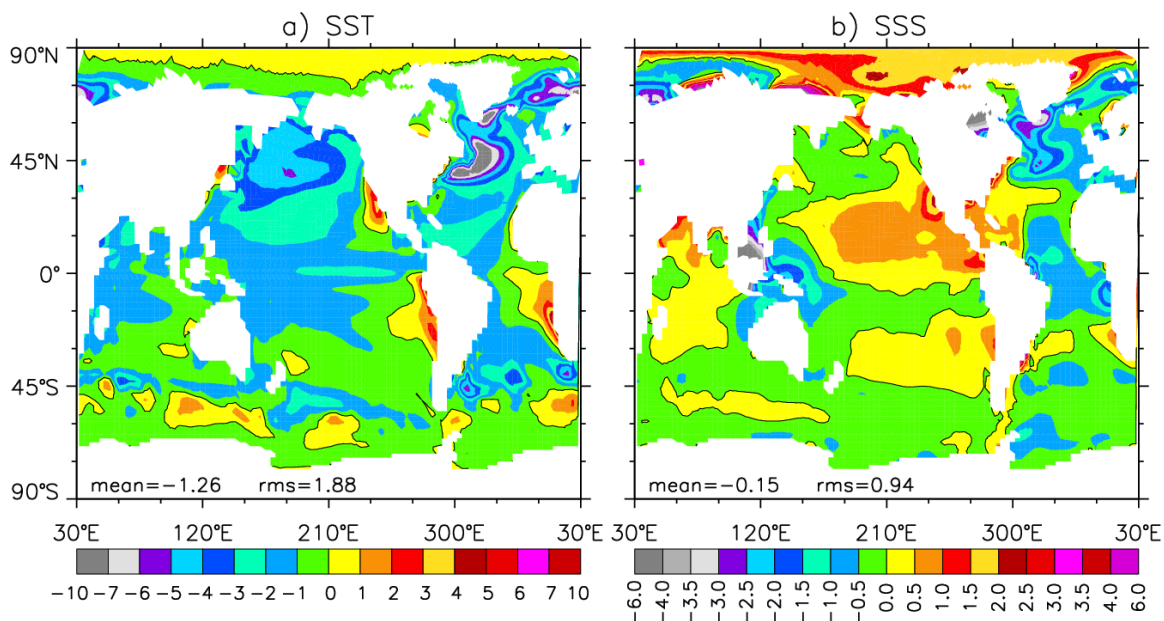


Figure 13. Sea surface a) temperature (SST, °C) and b) salinity (SSS, psu) T31x3_20C minus observations difference distributions. For temperature and salinity, the Hurrell et al. (2008) and PHC2 datasets are used, respectively.

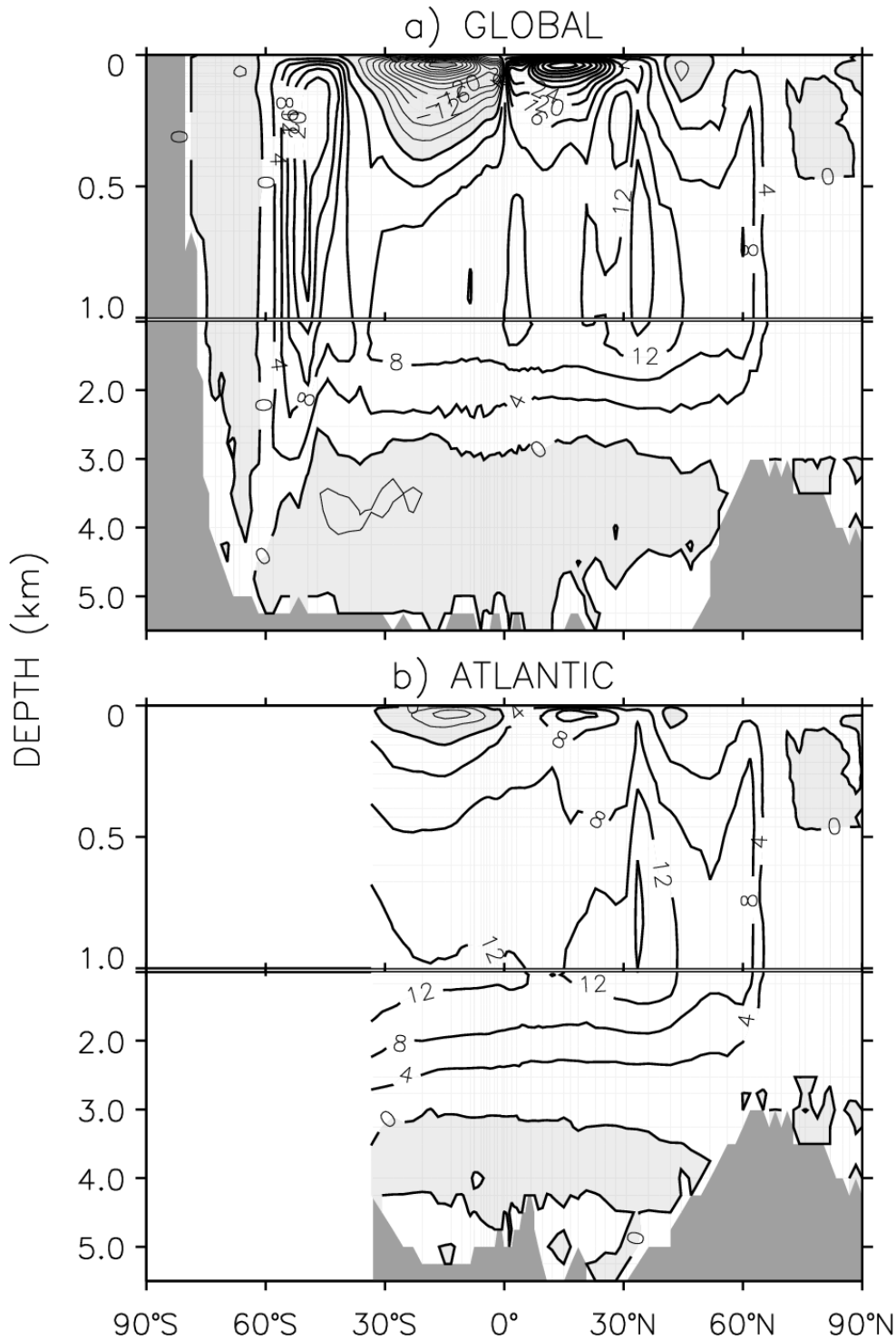


Figure 14. Meridional overturning circulation (Sv) for a) global and b) Atlantic Oceans from T31x3_20C. The plots represent the total overturning circulation that include the Eulerian-mean and parameterized mesoscale and submesoscale contributions. The positive and negative (shaded regions) contours denote clockwise and counter-clockwise circulations, respectively. The contour interval is 4 Sv.

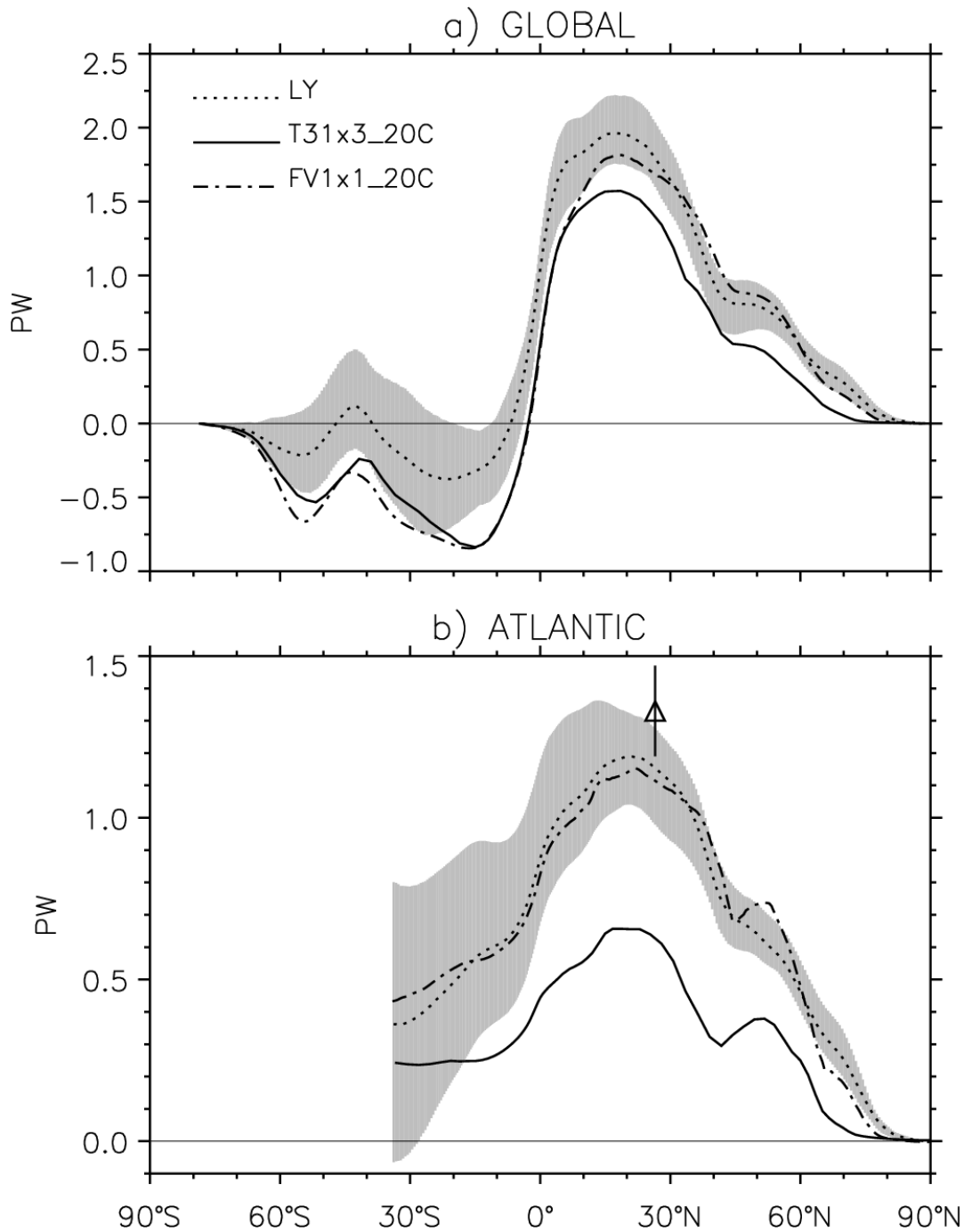


Figure 15. a) Global and b) Atlantic Ocean northward heat transports. The global transports are the total transports and include the parameterized mesoscale, submesoscale, and diffusive contributions as well as the Eulerian-mean component. The Atlantic Ocean transports exclude the diffusive component. The dotted line denoted by LY represents implied time-mean transport calculated by Large and Yeager (2009) with shading showing the implied transport range in individual years. The triangle with the error bar is an estimate based on the RAPID data from Johns et al. (2011).

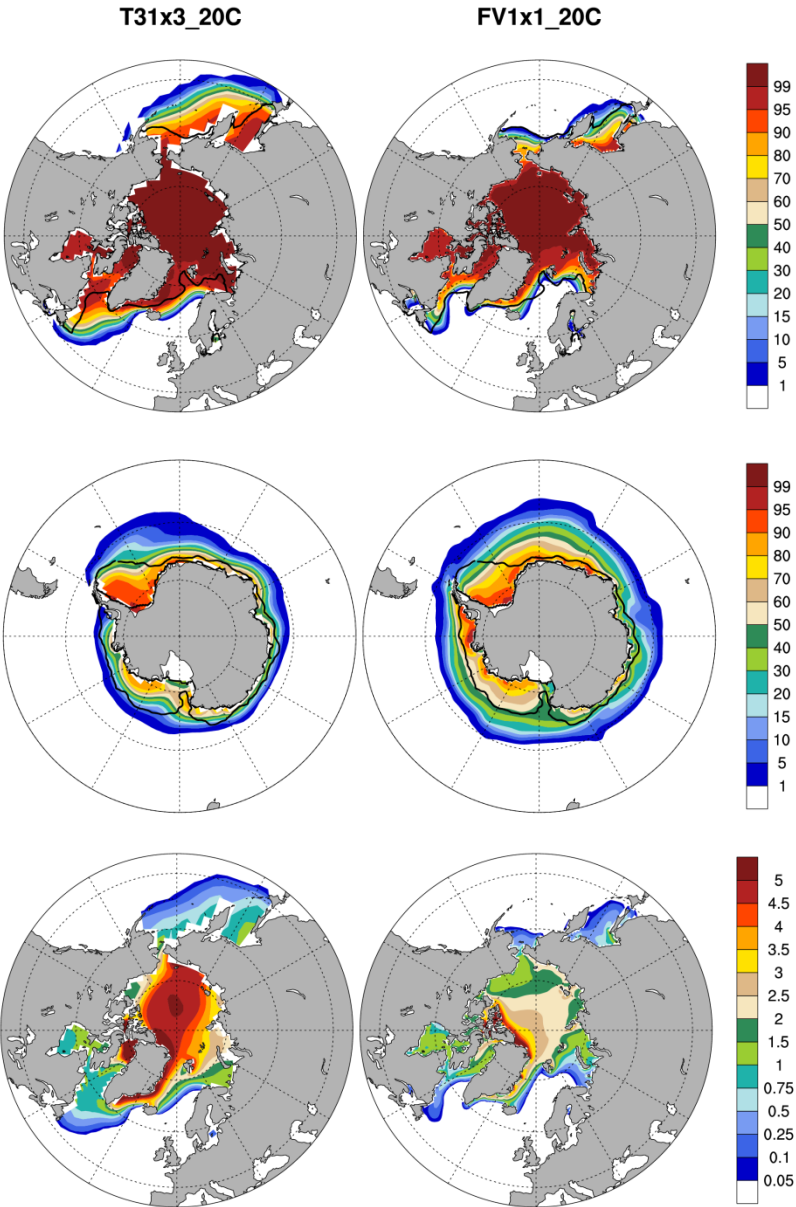


Figure 16. Northern Hemisphere JFM (winter) sea ice fraction (%) (upper panels) for T31x3_20C and FV1x1_20C. Southern Hemisphere JFM (summer) sea ice fraction (middle panels) (%) for T31x3_20C and FV1x1_20C. Northern Hemisphere JFM (winter) sea ice thickness (m) (lower panels) for T31x3_20C and FV1x1_20C. SSM/I observations for sea ice (10% concentration) are shown with heavy black line for reference.

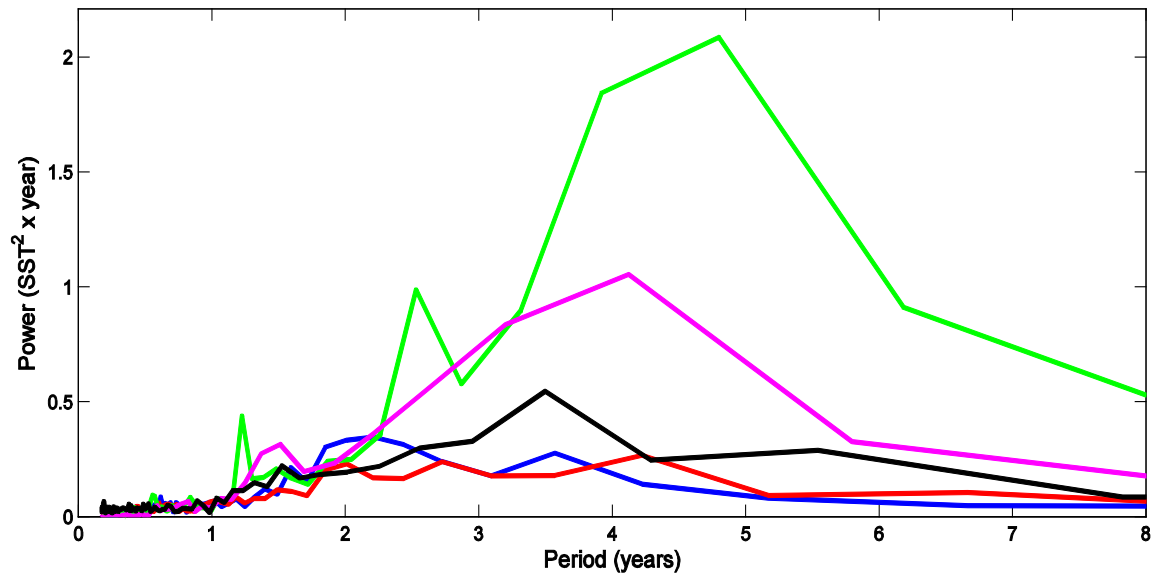


Figure 17 : Power spectrum for NINO3 SST anomalies for HadSST (black), T31x3_1850 (blue), T31x3_20C (red), FV2x1_1850 (green), and FV1x1_1850 (purple). The area under a line, when integrated across all periods, yields the total variance.

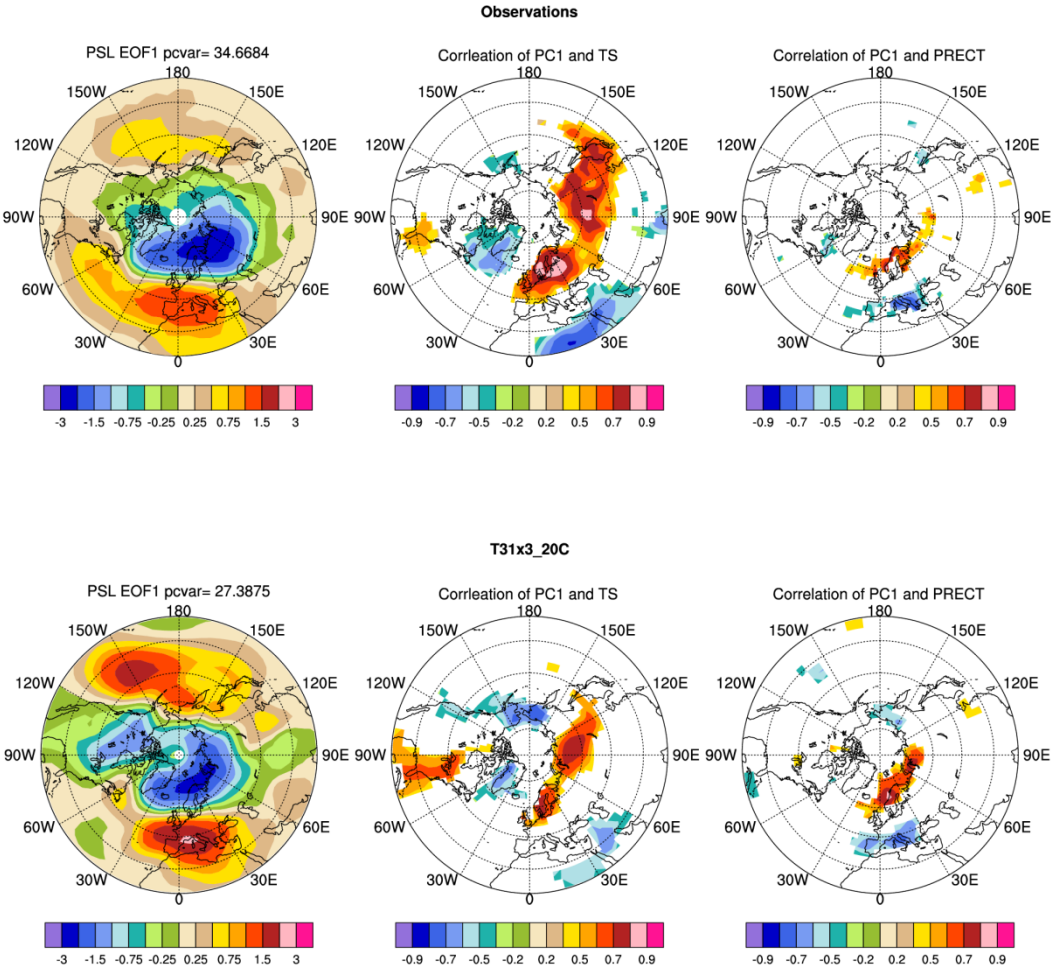


Figure 18. NAM analysis for T31x3_20C (lower panels) versus observations (upper panels). Winter (DJFM) PSL EOF1 (left) and correlations to surface temperature and precipitation anomaly timeseries (center and right). Observations include the Hadley Center mean sea level pressure dataset, NCEP mean monthly air temperature Reanalysis, and GPCP precipitation and all use years 1979-2008. Model data matches observational record for years 1979-2005. Correlations are plotted at the 95% significance level.

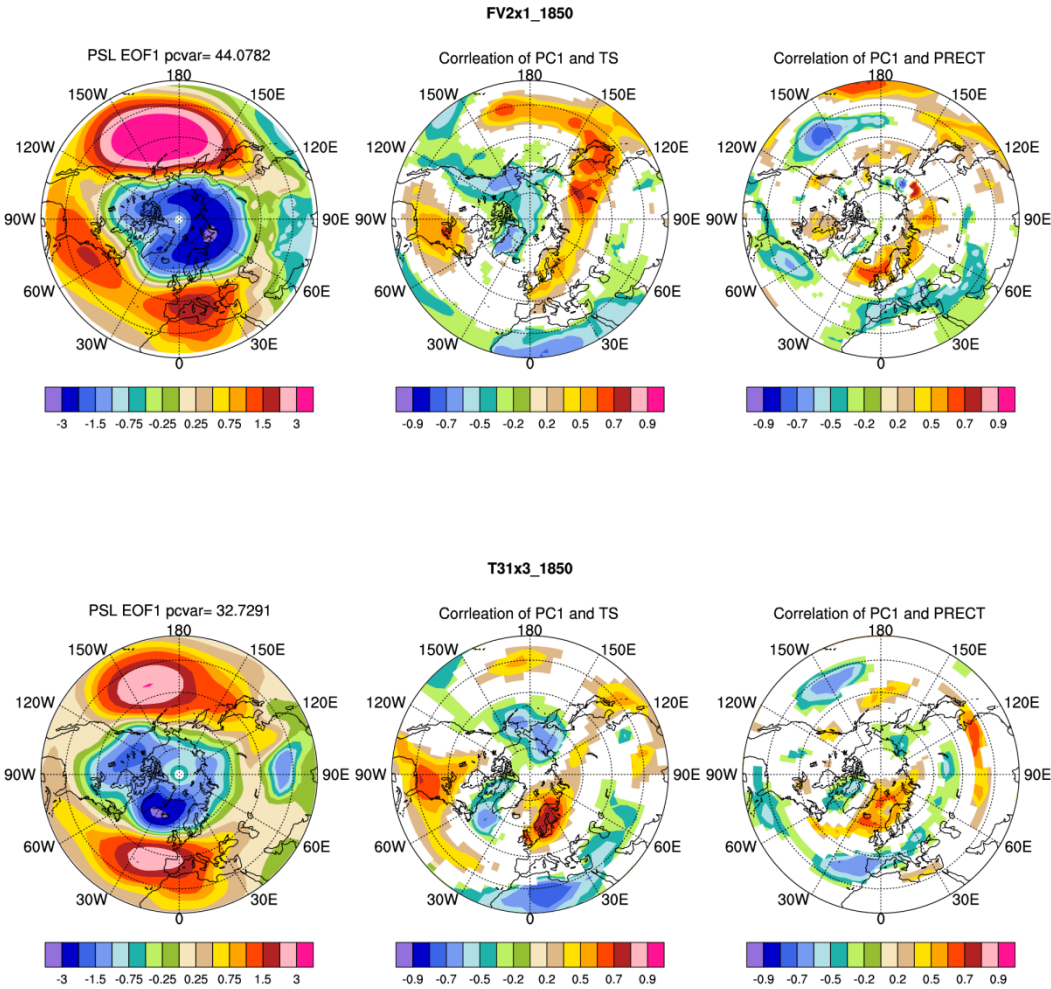


Figure 19. NAM analysis for T31x3_1850 (lower panels) versus FV2x1_1850 (upper panels). Winter (DJFM) PSL EOF1 (left) and correlations to surface temperature and precipitation anomaly timeseries (center and right). Model data uses the last 100 years of timeseries in the simulation. Correlations are plotted at the 95% significance level.

Table 1: NINO3 mean SST and standard deviation of the seasonal cycle and the interannual variability. All values are in °C.

Source	Mean	Seasonal Cycle	Interannual Variability
HadSST	25.7	0.95	0.79
T31x3_1850	24.0	1.08	0.65
T31x3_20C	24.1	1.03	0.69
FV2x1_1850	25.4	0.59	1.37
FV1x1_1850	25.4	0.72	1.02

Table 2: Low resolution (T31x3) CCSM4 performance on three typical platforms: an IBM Power 6; a Cray XT4; and a small Linux cluster. Top performance for each machine is highlighted in bold text. **FV2x1 and FV1x1 comparison figures are shown in italics. Note that T31x3 is not optimized for 512 or 576 pes.*

Machine	Processors (PES)	Simulated Years/Wallclock Day	Total Cost (PE-hours/Simulated Year)
CRAY XT4	420	64	157
CRAY XT4	220	54	98
CRAY XT4	120	41	70
Linux cluster	64	19	80
Linux cluster	48	18	66
Linux cluster	32	16	47
Linux cluster	16	10	38
IBM Power 6	576	<i>*FV2x1: 35</i>	<i>*FV2x1: 200</i>
IBM Power 6	512	<i>*FV1x1: 13</i>	<i>*FV1x1: 459</i>
IBM Power 6	192	72 <i>* FV2x1: 15</i>	32 <i>*FV2x1: 159</i>
IBM Power 6	128	49	31
IBM Power 6	64	32	24